Results in Physics 68 (2025) 108069

Contents lists available at ScienceDirect

Results in Physics

journal homepage: www.elsevier.com/locate/rinp

Exploring the implications of ternary Jeffrey nanofluid on pulsating flow and heat transfer through unsymmetrical corrugated micro conduit

Mohamed S. Abdel-wahed [a,b,*], Khaled S. Mekheimer [c], Ahmed Y. Sayed [d], Shaaban I. Ahmed [e]

[a] Department of Basic Engineering Sciences, Faculty of Engineering at Benha, Benha University, Cairo, Egypt
[b] Civil and Environmental Engineering Department, Collage of Engineering and Design, Kingdom University, Kingdom of Bahrain
[c] Department of Mathematics, Faculty of Science (Boys), Al-Azhar University, Cairo, Egypt
[d] Department of Engineering Mathematics and Physics, Faculty of Engineering El-Materia, Helwan University, Cairo, Egypt
[e] Department of Mathematics, Faculty of Science, Galala University, new galala city, Suez 43511, Egypt

ARTICLE INFO

Keywords:
Corrugated Microchannel
Jeffrey fluids
Ternary Nanofluid
Pulsating pressure

ABSTRACT

Pulsatile flow occurs in medical devices, impacting heat transfer and fluid behavior. It has practical significance in several disciplines, including thermodynamic devices. Pulses in flow and pressure influence pipe systems, reciprocating pumps, and compressors. Motivated by this, we simulated corrugated microchannel with Jeffery fluid flow enhanced by tri-nanoparticles to investigate this type of flow in detail. The model assumed that, in addition to external temperature influences, conduit walls experience electric and magnetic fields, governed by momentum and heat equations, along with electric potential and pulsing pressure equations. Using the perturbation method and Mathematica software, we derived semi-analytical solutions for the governing partial differential equations in their complex form. nanoparticle-enhanced blood exhibits improved thermal performance compared to pure fluid, with the type and concentration of nanoparticles (Fe_3O_4, Au, SWCNTs) significantly impacting heat dissipation and temperature distribution within the microfluidic conduit. Higher nanoparticle concentrations increase liquid viscosity, reducing velocity inside the conduit; however, a magnetic field can reverse this effect. This study underscores the application of pulsatile flow in heart pumps, where optimizing thermal characteristics can enhance device efficiency and patient outcomes.

Introduction

Distinguished by its simplicity, the Jeffery fluid is a non-Newtonian fluid. It uses time derivatives to characterize its behavior, as opposed to convected derivatives. Its linear viscoelastic characteristics make it very desirable for use in the polymer industry and other fields, these fluids are relevant in many different contexts. In order to understand the dynamics of blood flow, one must take into account viscoelastic behavior, which is related to Jeffrey fluid. *Hussain et al.* [1] analyzed the combined heat transfer for the Jeffery fluid's peristaltic transit in a curved channel while it is exposed to a magnetic strength and the implications of thermal radiation and Joule heating. *Kumar et al.* [2] simulated the motion of the blood flow inside irregular vertical peristaltic channel using Jeffrey model under the radiation effect. *Latha et al.* [3] Examined of the effects of heat dissipation on MHD peristaltic flow of Jeffery and Newtonian fluid through an asymmetric channel. *Manjunatha et al.* [4,5] investigated the impact of the Jeffery fluids' varying viscosity and thermal conductivity run within an inclined, axisymmetric, porous, uniform, or non-uniform tube. In order to investigate the effects of electroosmotic and wall properties of peristaltic microchannels filled with Jeffery liquid, *Rajashekhar et al.* [6] expanded on previous two researches. *Tanveer et al.* [7] examined the convective boundary conditions operating on a curved peristaltic duct filled with MHD Jeffery nanofluid.

Corrugated microchannels have attracted a lot of interest because of their many uses, in heat transfer and energy management Increasing miniaturization in industries including microelectronics, space applications, defense, and medical equipment has raised thermal load density. In order to ensure safe operation, corrugated microchannels are a useful way to quickly remove large heat loads from components. Numerous engineering and medicinal applications on the topic have been addressed in published literatures. The electroosmotic impact on the Jeffrey fluids in an opening microchannel was studied by *Liu et al.* [8]. The flow of nanofluids inside corrugated microchannels in the

* Corresponding author.
E-mail addresses: m.hassanin@ku.edu.bh, mohamed.sayed@bhit.bu.edu.eg (M.S. Abdel-wahed).

https://doi.org/10.1016/j.rinp.2024.108069
Received 16 September 2024; Received in revised form 6 November 2024; Accepted 3 December 2024
Available online 6 December 2024

Table 1
Blood and Nano particles physical characteristics.

Property	Base fluid/ Blood	Au	Fe_3O_4	SWCNTs
Density (kg/m^3)	1050	19300	7800	2600
Thermal conductivity (W/mk)	0.52	318	79.5	6600
Specific heat (j/kgK)	3617	129	461	425
Conductivity (s/m)	0.43	4.1×10^7	1×10^7	1×10^6
Thermal expansion coefficient $(1/k)$	0.18	1.4	20.6	27

presence of a magnetic force was studied by *Rashid et al.* [9]. The influence of coupled electromagnetohydrodynamic flow in a microchannel with a regular wavy rough wall through a porous material and its related heat transfer characteristics examined by *Reza et al.* [10]. The effects of single-walled carbon nanotube particles running inside a corrugated microchannel under the combined influence of electromagnetic and thermal forces were covered by *Sayed et al.* [11]. *Si et al.* [12] investigated the EMHD viscoelastic fluid over the microparallel corrugated panels under Lorenz force generated due to the combined influence of a horizontal electrical force and a vertical magnetic force. *Xuan et al.* [13] studied analytically the DC and AC electroosmotic flow in microchannels with arbitrary cross-sectional shape and arbitrary wall charge distribution.

Unique characteristics of nanofluids rendering them potentially valuable in a range of applications, including transfer of heat. They outperform the base fluid in terms of convective heat transfer coefficient and thermal conductivity. Applications include anything from fuel cells and microelectronics to pharmaceutical manufacturing and hybrid power plants. *Abdel-Wahed and others* [14–21] investigated a number of models used with nanofluids, assessing the impact of these models on the physical and thermal characteristics as well as how these characteristics reflected in the mechanical characteristics of certain models, including stiffness, hardness, ductility, and strength. They evaluated the heat treatment procedures used on flat, cylindrical, and disc surfaces as a means of applying the cooling process, as well as the rate at which this type of fluids improved these characteristics. *El-Bashbeshy et al.* [22] Examined the unsteady nanofluid flow over a moving cylinder subjected to several thermal forces and their impact on the mechanical properties. *Mohammadein et al.* [23] suggested KKL model to investigate the flow and heat transfer of the boundary layer over a moving plate exposed to magnetic force and nonlinear thermal radiation. *Raslan et al.* [24] used a combination of nanofluids and micropolar fluids as a cooling mixing for a flat surface exposed to a magnetic field. On the same model as Raslan, *Sayed et al.* [25] studied entropy and the extent to which it was affected by this mixture of fluids in the presence of different thermal influences.

A blend that includes two/three distinct types of nanoparticles is called a ternary nanofluid. A base fluid's unique features and behavior can result from the mixing of several types of nanoparticles, such as metallic, non-metallic, and carbon nanotubes. Plastic films, heat exchangers, glass fiber, petroleum products, polymer sheets, and electronic gadgets are among the items made with these nanofluids [26–31].

In fluid dynamics, periodic fluctuations in flow result in pulsating flow commonly referred to as Womersley flow, the Fluid motion with regular oscillations is referred to as pulsating flow. These differences may be caused by internal (such as blood flow in arteries) or external (such as rotating mechanisms) influences. For cardiovascular systems, pulsatile flow is typical in animals with circulatory systems (such as humans) because of the heart's regular pumping action. Moreover Hydraulic systems and engines, Fluid flow pulsations can be produced by rotating machinery. *Ali et al.* [32] examined the pulsating flow of NNF (micropolar-Casson) in a narrow, porous channel with applying of - magnetic field. *Kannaiah et al.* [33] Conducted a numerical investigation of the effect of pulsing pressure on blood flow when Fe_2O_3 nanoparticles are positioned inside a vertical channel. *Somasundaram et al.* [34] demonstrated the magnetohydrodynamic pulsing flow of blood-carrying Al_2O_3 nanoparticles in a channel, including the influence of viscous dissipation and Joule heating effects. *Subramanyam et al.* [35] compared the pulsating pressure impact on two different types of hybrid nanoparticle (Au + SWCNT)/ (Au + MWCNT) that support blood flowing in a porous vertical channel. *Sayed et al.* [36] examined the flow behavior of the blood under the effect of pulsating pressure running inside Corrugated unsymmetrical microchannel. More publications discuss the impact of nanofluids founded in [37–40].

The intent of this work is to investigate the impact of blood supported by three kinds of nano particles on the flow and heat transfer within a micro- corrugated conduit under the influence of pulsating pressure, electric and magnetic fields, and other factors after reviewing prior literature to ensure the work novelty. Using the governing flow equations in their partial differential form as a model, the issue was solved analytically based on the perturbation approach.

Physical simulation of the issue

Suppose a 3-Dimensinoal incompressible, unsteady, laminar, electrically conducting Jeffrey fluid flow supported with three types of nanoparticles (Au, Fe_3O_4, and SWCNTs) with base fluid (Blood) density ρ_f, electrical conductivity σ running between two fixed corrugated walls (Table 1). The height of the walls assumed $2H$, such that the typical height of $H \cong 100\mu m$, the layer thickness W where $L \gg H$, the amplitude of the corrugated wall is $0.1H$, representing a geometric deformation in microchannels fabricated using precise manufacturing techniques [12]. The undulations of the upper and lower walls of the channel change according to the following equations [36], Refer to Fig. 1.

$$y_u^* = d_1^* + a_1^* \sin\left(\frac{\lambda x^*}{d_1}\right), y_l^* = -d_2^* + a_2^* \sin\left(\frac{\lambda x^* + \theta^*}{d_1}\right) \tag{1}$$

The amplitude of the waves is represented by a_1 and a_2, λ is the wave number and the width of the channel by $H = d_1 + d_2$. The phase difference between the two corrugated walls is denoted by θ^*. Moreover, the variables a_1^*; a_2^*; d_1^*; d_2^* satisfy the condition [41–43]

$$a_1^{*2} + a_2^{*2} + 2a_1^* a_2^* \cos\theta \le \left(d_1^* + d_2^*\right)^2 \tag{2}$$

Distribution of electric potential

To determine the net charge density ρ_e within the Electric Debye length (EDL) in a conduit with a corrugated wall, we first calculate the EDL potential $\psi^* = \psi^*(x,y)$. The electric field E is given by $E = -\nabla\psi^*$, and the divergence of E is $\nabla \bullet E = \rho_e/\epsilon_0$, which leads to Poisson's equation $\nabla^2\psi^* = -\rho_e/\epsilon_0$. Therefore,

$$\rho_e = -\epsilon_0 \nabla^2 \psi^* = -2ez_0 n_0 \, sinh\left(\frac{ez_0\psi^*}{k_B T_a}\right), \tag{3}$$

where $n_0, e_0, z_0, T_a, \epsilon_0$, and k_B represent the ion density, electronic charge, valence, absolute temperature, the solution's permittivity constant and Boltzmann constant, respectively.

Assuming that ψ^* is very small, the term $(ez_0\psi^*/k_B T_a) \ll 1$ allows us to approximate the term $\left(sinh\frac{ez_0\psi^*}{k_B T_a}\right)$

$$\nabla^2\psi^* = k^2\psi^* \tag{4}$$

where $k = ez_0\sqrt{\frac{2n_0}{\epsilon_0 k_B T_a}}$ is the Debye–Hückle parameter.

The boundary conditions at the walls become:

$$\psi^* = \zeta \; at \; y_u^* = d_1 + a_1 \sin\left(\frac{\lambda x^*}{d_1}\right), \; y_l^* = -d_2 + a_2 \sin\left(\frac{\lambda x^* + \theta^*}{d_1}\right) \tag{5}$$

The non-dimensional variables are defined as:

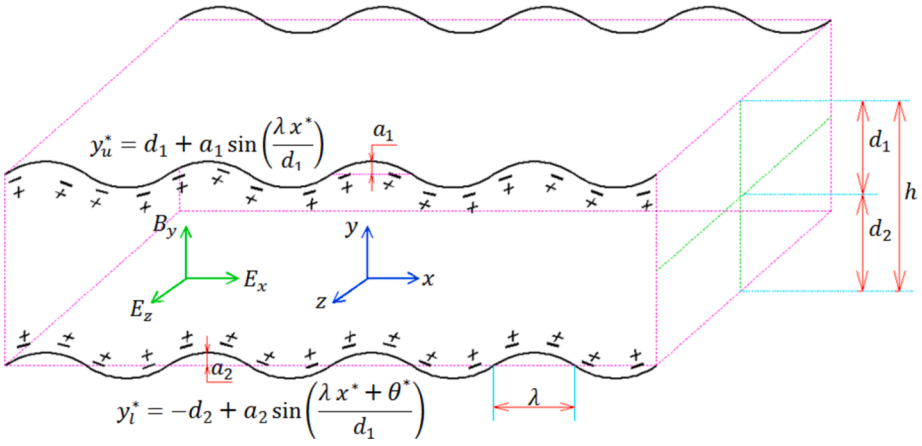

Fig. 1. The problem's geometry and physical aspects.

$$\psi = \frac{\psi^*}{\zeta}, x = \frac{x^*}{d_1}, y = \frac{y^*}{d_1}, \theta = \frac{\theta^*}{d_1}, d_2 = \alpha d_1, a_2 = \gamma a_1, a_1 = \varepsilon d_1 \tag{6}$$

Here α is height ratio, γ is amplitude ratio, and where ε is small amplitude.

by assuming that the potential ζ remains constant, in order to make the linearized Poisson equation dimensionless, by substitute the non-dimensional variables into Equation (4).

$$\nabla^2\psi = \beta^2\psi \tag{7}$$

In this context,$\beta = kH$ represents the normalized reciprocal thickness of the electric double layer (EDL), indicating the ratio between the microchannels half height and the Debye length $(1/k)$. And the dimensionless boundary conditions for the electrical potential can be defined as follows:

$$\psi = 1 \ at \ y_u = 1 + \varepsilon\sin(\lambda x), \tag{8}$$

$$\psi = 1 \ at \ y_l = -\alpha + \gamma \ \varepsilon \ \sin(\lambda x + \theta). \tag{9}$$

The electric potential function is described by the regular perturbation expansion at small values of ε.

$$\psi(x,y) = \psi_o(x,y) + \varepsilon\psi_1(x,y) + \varepsilon^2\psi_2(x,y) + \ldots\ldots\ldots \tag{10}$$

$$\varepsilon^2 : \begin{cases} \psi_2(x,y)\,|_{y=1} = -sin(\lambda x)\dfrac{\partial\psi_1(x,y)}{\partial y}\bigg|_{y=1} - \dfrac{sin^2(\lambda x)}{2}\dfrac{\partial^2\psi_o(x,y)}{\partial y^2}\bigg|_{y=1} \\ \psi_2(x,y)\,|_{y=-\alpha} = -\gamma sin(\lambda x+\theta)\dfrac{\partial\psi_1(x,y)}{\partial y}\bigg|_{y=-\alpha} - \gamma^2\dfrac{sin^2(\lambda x+\theta)}{2}\dfrac{\partial^2\psi_o(x,y)}{\partial y^2}\bigg|_{y=-\alpha} \end{cases} \tag{18}$$

By substituting Eq. (10) into Eq. (7), we get

$$\varepsilon^0 : \frac{\partial^2\psi_o}{\partial x^2} + \frac{\partial^2\psi_o}{\partial y^2} - \beta^2\psi_o = 0, \tag{11}$$

$$\varepsilon^1 : \frac{\partial^2\psi_1}{\partial x^2} + \frac{\partial^2\psi_1}{\partial y^2} - \beta^2\psi_1 = 0, \tag{12}$$

$$\varepsilon^2 : \frac{\partial^2\psi_2}{\partial x^2} + \frac{\partial^2\psi_2}{\partial y^2} - \beta^2\psi_2 = 0. \tag{13}$$

A Taylor series around the mean wall locations can be used to expand the boundary restrictions equations (8) and (9) as follows. $y = 1$ and $y = -\alpha$.

$$1 = \psi(x,1) + \varepsilon\sin(\lambda x)\frac{\partial\psi}{\partial y}(x,1) + \frac{\varepsilon^2}{2}\sin^2(\lambda x)\frac{\partial^2\psi}{\partial y^2}(x,1) + \ldots\ldots\ldots \tag{14}$$

$$1 = \psi(x,-\alpha) + \gamma\,\varepsilon\,\sin(\lambda x+\theta)\frac{\partial\psi}{\partial y}(x,-\alpha) + \gamma^2\frac{\varepsilon^2}{2}\sin^2(\lambda x+\theta)\frac{\partial^2\psi}{\partial y^2}(x,-\alpha) + \ldots\ldots\ldots \tag{15}$$

Similarly, combining terms with equal powers can further simplify the corresponding boundary conditions provided by equations (11), (12), and (13), as seen below.

$$\varepsilon^o : \begin{cases} \psi_o(x,y)\,|_{y=1} = 1 \\ \psi_o(x,y)\,|_{y=-\alpha} = 1 \end{cases} \tag{16}$$

$$\varepsilon^1 : \begin{cases} \psi_1(x,y)\,|_{y=1} = -\sin(\lambda x)\dfrac{\partial\psi_o(x,y)}{\partial y}\bigg|_{y=1} \\ \psi_1(x,y)\,|_{y=-\alpha} = -\gamma\sin(\lambda x+\theta)\dfrac{\partial\psi_o(x,y)}{\partial y}\bigg|_{y=-\alpha} \end{cases} \tag{17}$$

Equations (11) and (16) provide us with

$$\psi_o(y) = \frac{e^{(y+\alpha)\beta} + e^{\beta-y\beta}}{1 + e^{\beta+\alpha\beta}} \tag{19}$$

Equations (12) and (17) provide us with.

$$\psi_1(x,y) = \frac{1}{2}e^{-yG_1}(-1+\coth((1+\alpha)G_1))\begin{Bmatrix} c_1\sin(x\lambda)\left(e^{G_1} - e^{(1+2y+2\alpha)G_1}\right) \\ +c_2\sin(x\lambda)\left(-e^{(2+\alpha)G_1} + e^{(2y+\alpha)G_1}\right)\gamma\cos\theta \\ +c_2\gamma\,\mathrm{csch}((1+\alpha)G_1)\sin\theta\sinh((-1+y)G_1)\cos(x\lambda) \end{Bmatrix} \tag{20}$$

Equations (13) and (18) provide us with

Table 2
Typical values of the physical variables [8,12].

Physical variables	Values [units]
Characteristic channel length (H)	$40\mu m$
Charge of the photon (e)	$1.6\times10^{-19}C$
Electrical potential at the wall (ξ)	$-12Vm$
Electrical field in axial direction (E_x)	$0-2\times10^{4}V/m$
Electrical field in transverse direction (E_z)	$0-2\times10^{4}V/m$
Applied magnetic field (B_y)	$1-50T$
Boltzmann constant (k_B)	$1.38\times10^{-23}J/K$
Ion density (n_0)	$1mol/m^3$
Valence of ions (z)	1
Permittivity of the fluid (ϵ_0)	$5.3\times10^{-10}C/Vm$
Viscosity of the fluid (μ)	$10-6m^2/s$
Permeability of porous media (K)	$0-10^{-11}m^2$
Electrical conductivity (σ_e)	$1000W/m^2$

Table 3
Comparison of numerical values of volumetric flow rate (Real numbers) for different Hartmann number (Ha).

Ha	D. Si and Y. Jian [12]		Present work	Present work
	$q(1)$	$q(60)$	$q(1)$	$q(60)$
0	0.00031	0.00029	0.00030	0.00030
0.01	0.310328	0.30301	0.30510	0.30487
0.5	7.96014	7.95533	7.96214	7.95657
0.75	7.49333	7.48907	7.49747	7.49279
1	6.61813	6.58953	6.60208	6.59863
2	4.10098	4.10179	4.10174	4.10250
3	2.92822	2.93058	2.93280	2.93727

$$\psi_2(x,y)=\frac{1}{8}e^{-y\beta}(-1+\coth((1+\alpha)\beta]))\Big(-\left(e^{\beta}+e^{(2y+\alpha)\beta}\right)\Big(-1+e^{\beta+\alpha\beta}\Big)\beta^2-2e^{\beta}\Big(-1+e^{2(y+\alpha)\beta}\Big)c_3-2\Big(e^{(2+\alpha)\beta}-e^{(2y+\alpha)\beta}\Big)(\cos(\theta)\,c_4+\sin(\theta)c_6)\Big)+\frac{1}{8}e^{-yG_2}(-1+\coth((1+\alpha)G_2))\left(\beta^2\left(\left(e^{(2+\alpha)G_2}-e^{(2y+\alpha)G_2}\right)\cos(2\theta)+2e^{(1+y+\alpha)G_2}\sinh((y+\alpha)G_2)\right)+4e^{(1+y+\alpha)G_2}\sinh((y+\alpha)G_2)\,c_3+2\Big(e^{(2+\alpha)G_2}-e^{(2y+\alpha)G_2}\Big)(\cos(\theta)\,c_4-\sin(\theta)\,c_6)\right)\mathrm{Cos}(2x\lambda)+\frac{1}{4}e^{-yG_2}(-1+\coth((1+\alpha)G_2))\Big(\left(-e^{(2+\alpha)G_2}+e^{(2y+\alpha)G_2}\right)\sin(\theta)c_4+e^{(1+y+\alpha)G_2}\Big(-2\sinh((y+\alpha)G_2)c_5+2\cos(\theta)\sinh[(-1+y)G_2]\left(\beta^2\sin(\theta)+c_6\right)\Big)\Big)\sin(2x\lambda) \tag{21}$$

where $G_1, G_2, c_1, c_2, c_3, c_4, c_5$ and c_6 are defined in appendix A.

The Mathematica software helps to properly solve the equations (11–13) and associated boundary conditions (16–18) by using the *DSolve* function. Using Eq. (10), we can deduce the overall solution for the potential equation by getting $\psi_o(x,y), \psi_1(x,y), \text{and}\psi_2(x,y)$.

Flow velocity distribution

The equations describing the continuity and momentum balance for a Jeffrey fluid can be expressed as follows:

$$\nabla\bullet\vec{V}=0 \tag{22}$$

$$\rho_{thnf}\frac{\partial\vec{V}}{\partial t}+\rho_{thnf}\left(\vec{V}\bullet\nabla\right)\vec{V}=\rho_{thnf}g-\nabla P+\mu_{thnf}\nabla\tau^{*}+\vec{F}-\frac{\mu}{k}\vec{V} \tag{23}$$

where:

$$\vec{F}=\vec{J}\times\vec{B}+\rho_e\vec{E}. \tag{24}$$

In Equation (21), ρ_e and $\vec{E}$ represent the net electric charge density and the applied electric field, respectively. F represents the Lorentz force, which arises from the interaction between fluid flow and the applied magnetic field. In this case, the magnetic field acts in the y-direction as $\vec{B}=B_0\vec{e}_y$, and the uniform electric field is given by $\vec{E}=E_x\vec{e}_x+E_z\vec{e}_z$. Additionally, the electric current density $\vec{J}$ is expressed as $\vec{J}=\sigma_{thnf}\left[\vec{V}\times\vec{B}\right]+\sigma_{thnf}\vec{E}$, where $\vec{E}$ is caused by an $x-$ directional electric field *Rashid and Nadeem* [13]. Based on the aforementioned assumption, only the velocity component $w^{*}(x,y)$ along the $z^{*}-$ axis will be preserved, and it remains independent of z^{*} as dictated by the continuity equation (21). As a result, equation (22) can be simplified as follows:

$$\rho_{thnf}\frac{\partial w^{*}}{\partial t^{*}}=\frac{\partial\tau^{*}_{x^{*}z^{*}}}{\partial x^{*}}+\frac{\partial\tau^{*}_{y^{*}z^{*}}}{\partial y^{*}}+\frac{\partial\tau^{*}_{z^{*}z^{*}}}{\partial z^{*}}-\frac{\partial P}{\partial z}-\sigma_{thnf}w^{*}B_o^2+\sigma_{thnf}E_xB_o+\rho_eE_z-\frac{\mu_{thnf}}{k}w^{*} \tag{25}$$

The constitution relation of Jeffrey fluid *Liu et al.* [14] satisfies:

$$\tau^{*}_{ij}+\lambda_1\frac{\partial\tau^{*}_{ij}}{\partial t^{*}}=\mu_{thnf}\left(\gamma^{*}_{ij}+\lambda_2\frac{\partial\gamma^{*}_{ij}}{\partial t^{*}}\right) \tag{26}$$

The stress tensor τ^{*}_{ij} represents the stress in the nanofluid, while μ_{thnf} denotes the variable viscosity of the Ternary Jeffrey fluid. The relaxation time λ_1 and the retardation time λ_2 are parameters that describe the

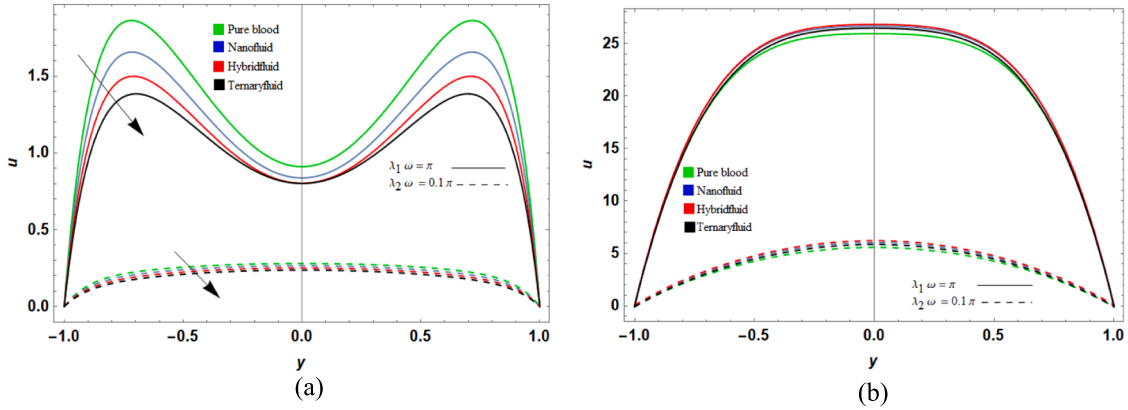

$$at\ \varepsilon=0.1,\theta=0,\pi\ ,\lambda=0.1,\gamma=1,\alpha=1,\mathrm{Re}=2,\beta=10,\mathrm{Da}=\infty,x=0,Ha=1.5,\tau=2$$
$$(\boldsymbol{a})\ s=0\ ,\qquad (\boldsymbol{b})s=50$$

Fig. 2. Velocity variation vs. the nanoparticles concentration.

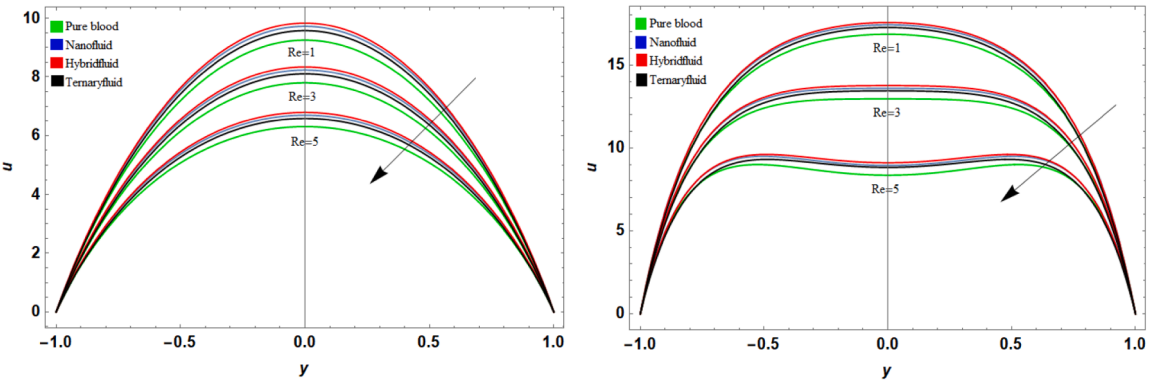

$at\ \varepsilon = 0.1, \theta = 0, \pi, \lambda = 0.1, \gamma = 1, \alpha = 1, \beta = 10, \mathrm{Da} = 0.5, x = 0, Ha = 1.5, \tau = 2, s = 50$

$(\boldsymbol{a})\ \omega\lambda_1 = 0.5\pi, \omega\lambda_2 = 1.5\pi \qquad (\boldsymbol{b})\ \omega\lambda_1 = 1.5\pi, \omega\lambda_2 = 0.5\pi$

Fig. 3. Velocity variation vs. the nanoparticles concentration.

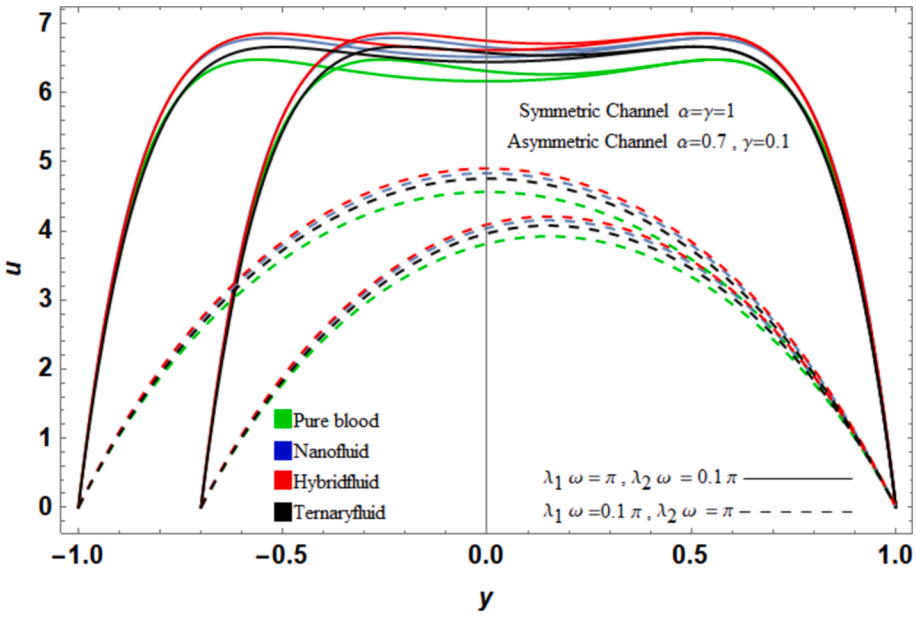

Fig. 4. Velocity variation vs. height ratio α and amplitude ratio γ at $\theta = 0, \pi$ pure fluid, $\varepsilon = 0.1, \lambda = 0.1, \mathrm{Re} = 2, \beta = 10, \mathrm{Da} = 0.1, s = 50, Ha = 1.5, \tau = 2$.

behavior of the fluid. The strain tensor is defined as $\gamma_{ij}^{*} = \frac{\partial u_j^{*}}{\partial x_i^{*}}$. Additionally, μ represents the zero-shear rate viscosity.

The boundary conditions for the problem can be expressed as follows:

$$w^{*}(x^{*}, y_u^{*}) = w^{*}(x^{*}, y_l^{*}) = 0 \tag{27}$$

We made the assumption that the liquid flowing through the microchannel is an incompressible fluid. Moreover, we only considered the flow in the Z* direction. Additionally, the velocity of the fluid satisfies the condition that the pressure gradient in the $z^{*}-$ direction is periodic over time.

$$\left(1+\lambda_1\frac{\partial}{\partial t^{*}}\right)\left[\rho_{thnf}\frac{\partial w^{*}}{\partial t^{*}}+\frac{\partial \mathrm{P}}{\partial z^{*}}+\sigma_{thnf}w^{*}B_o^2-\sigma_{thnf}E_xB_o-\rho_eE_z+\frac{\mu_{thnf}}{k}w^{*}\right]$$
$$=\mu_{thnf}\left(1+\lambda_2\frac{\partial}{\partial t^{*}}\right)\left(\frac{\partial^2 w^{*}(x^{*},y^{*})}{\partial x^{*2}}+\frac{\partial^2 w^{*}(x^{*},y^{*})}{\partial y^{*2}}\right) \tag{28}$$

Where assuming that the pressure gradient and velocity and electric field are write as [39,40]:

$$\frac{\partial \mathrm{P}}{\partial z^{*}} = -\frac{\mu_{thnf}\omega k_1 \cos\omega t^{*}}{d_1} = -\frac{\mu_{thnf}\omega\tau}{d_1}\Re\left\{e^{i\omega t^{*}}\right\}$$

$$w^{*} = \Re\left\{u^{*}(x^{*},y^{*})e^{i\omega t^{*}}\right\}, E_x = \Re\left\{E_0 e^{i\omega t^{*}}\right\}, E_z = \Re\left\{E_0 e^{i\omega t^{*}}\right\}$$

By introducing the following dimensionless variables and substituting them into Equation (26),

$$u = \frac{u^{*}(x^{*},y^{*})}{d_1\omega}, Ha^2 = \frac{B_o^2 d_1^2\sigma}{\mu_f}, S = \frac{E_0}{\omega}\sqrt{\frac{\sigma_f}{\mu_f}}, Re = \frac{\rho_f\omega d_1^2}{\mu_f}, Da = \frac{k}{d_1^2}$$

$$\frac{\partial^2 u}{\partial x^2}+\frac{\partial^2 u}{\partial y^2}-Bu-p+\delta\psi = 0 \tag{29}$$

with the following boundary conditions:

$$u = 0\ at\ y_u = 1+\varepsilon\sin(x\lambda) \tag{30}$$

$$u = 0\ at\ y_l = -\alpha+\gamma\,\varepsilon\sin(\lambda x+\theta) \tag{31}$$

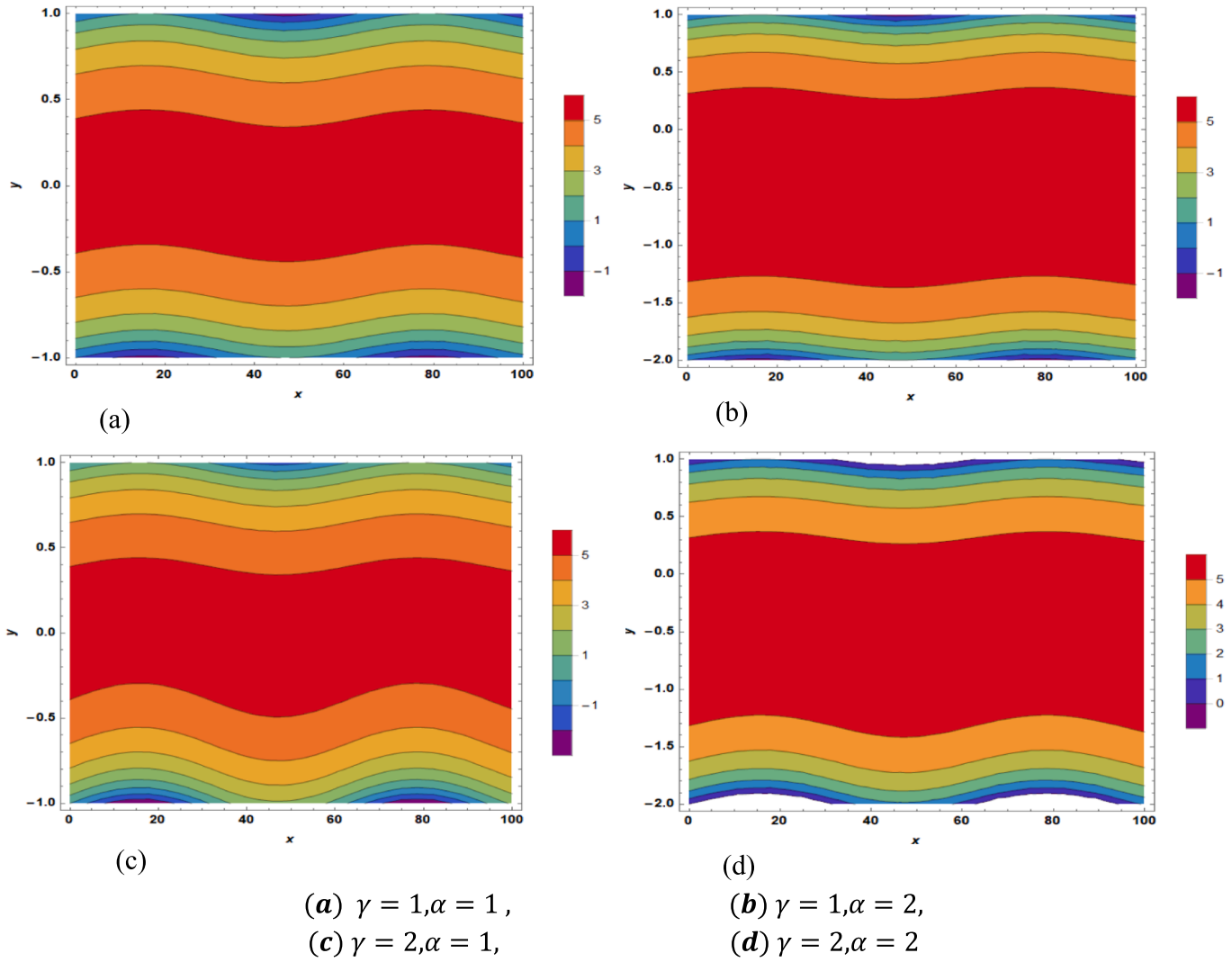

$(\boldsymbol{a})\ \gamma = 1, \alpha = 1$, $(\boldsymbol{b})\ \gamma = 1, \alpha = 2$,
$(\boldsymbol{c})\ \gamma = 2, \alpha = 1$, $(\boldsymbol{d})\ \gamma = 2, \alpha = 2$

Fig. 5. Velocity contour variation vs. height ratio α and amplitude ratio γ at $\theta = 0$, pure fluid, $\varepsilon = 0.05, \lambda = 0.1, \mathrm{Re} = 1, \beta = 10, \mathrm{Da} = 0.5, s = 25, Ha = 0.5, \tau = 1$, $\omega\lambda_1 = 0.5\pi, \omega\lambda_2 = 0.1\pi$.

where:

$$\left.\begin{aligned} A = \frac{(1+i\omega\lambda_1)}{(1+i\omega\lambda_2)}, B = A(i)Re + A\left(\frac{A_2}{A_1}\right)Ha^2 + A\left(\frac{1}{Da}\right), \\ p = -A\tau - A\left(\frac{A_2}{A_1}\right)Hs, \delta = A\left(\frac{1}{A_1}\right)\beta^2, Hs = Ha^*S \\ A_1 = \frac{\mu_{thnf}}{\mu_f} = \frac{1}{(1-\phi_1)^{2.5}(1-\phi_2)^{2.5}(1-\phi_3)^{2.5}}, A_2 = \frac{\sigma_{thnf}}{\sigma_f} \\ \sigma_{nf} = \sigma_f\left(\frac{(1+2\phi_3)\sigma_{s3} + (1-2\phi_3)\sigma_f}{(1-\phi_3)\sigma_{s3} + (1+\phi_3)\sigma_f}\right), \\ \sigma_{hnf} = \sigma_{nf}\left(\frac{(1+2\phi_2)\sigma_{s2} + (1-2\phi_2)\sigma_{nf}}{(1-\phi_2)\sigma_{s2} + (1+\phi_2)\sigma_{nf}}\right), \\ \sigma_{thnf} = \sigma_{hnf}\left(\frac{(1+2\phi_1)\sigma_{s1} + (1-2\phi_1)\sigma_{hnf}}{(1-\phi_1)\sigma_{s1} + (1+\phi_1)\sigma_{hnf}}\right) \end{aligned}\right\} \quad (32)$$

Where ϕ_1, ϕ_2 and ϕ_3 represennt the concentrations of single-walled carbon nanotubes, Iron oxide nanoparticles and gold nanoparticles, respectively.

The regular perturbation expansion in small values of ε can be used to describe the velocity.

$$u(x,y) = u_o(x,y) + \varepsilon\, u_1(x,y) + \varepsilon^2\, u_2(x,y) + \ldots\ldots\ldots\ldots \quad (33)$$

By substituting Eq. (30) into Eq. (27), we get

$$\varepsilon^o : \frac{\partial^2 u_o}{\partial x^2} + \frac{\partial^2 u_o}{\partial y^2} - Bu_o + \delta\psi_o = p \quad (34)$$

$$\varepsilon^1 : \frac{\partial^2 u_1}{\partial x^2} + \frac{\partial^2 u_1}{\partial y^2} - Bu_1 + \delta\psi_1 = 0 \quad (35)$$

$$\varepsilon^2 : \frac{\partial^2 u_2}{\partial x^2} + \frac{\partial^2 u_2}{\partial y^2} - Bu_2 + \delta\psi_2 = 0 \quad (36)$$

The boundary constraints equations (29) and (30) can be expanded in the following form using a Taylor series around the mean wall positions $y = 1$ and $y = -\alpha$.

$$0 = u(x,1) + \varepsilon \sin(\lambda x)\frac{\partial u}{\partial y}(x,1) + \frac{\varepsilon^2}{2}\sin^2(\lambda x)\frac{\partial^2 u}{\partial y^2}(x,1) + \ldots\ldots\ldots \quad (37)$$

$$0 = u(x,-\alpha) + \gamma\,\varepsilon\,\sin(\lambda x+\theta)\frac{\partial u}{\partial y}(x,-\alpha) + \gamma^2\frac{\varepsilon^2}{2}\sin^2(\lambda x+\theta)\frac{\partial^2 u}{\partial y^2}(x,-\alpha) + \ldots\ldots\ldots \tag{38}$$

Similarly, the associated boundary conditions given by equations (32), (33), and (34) can be further simplified by grouping terms with equal powers, as shown below.

$$\varepsilon^o\begin{cases} u_o(x,y)\,|_{y=1} = 0 \\ u_o(x,y)\,|_{y=-\alpha} = 0 \end{cases} \tag{29}$$

$$\varepsilon^1:\begin{cases} u_1(x,y)\,|_{y=1} = -\sin(\lambda x)\dfrac{\partial u_o(x,y)}{\partial y}\Big|_{y=1} \\ u_1(x,y)\,|_{y=-\alpha} = -\gamma\sin(\lambda x+\theta)\dfrac{\partial u_o(x,y)}{\partial y}\Big|_{y=-\alpha} \end{cases} \tag{40}$$

$$\varepsilon^2:\begin{cases} u_2(x,y)\,|_{y=1} = -sin(\lambda x)\dfrac{\partial u_1(x,y)}{\partial y}\Big|_{y=1} - \dfrac{sin^2(\lambda x)}{2}\dfrac{\partial^2 u_o(x,y)}{\partial y^2}\Big|_{y=1} \\ u_2(x,y)\,|_{y=-\alpha} = -\gamma sin(\lambda x+\theta)\dfrac{\partial u_1(x,y)}{\partial y}\Big|_{y=-\alpha} - \gamma^2\dfrac{sin^2(\lambda x+\theta)}{2}\dfrac{\partial^2 u_o(x,y)}{\partial y^2}\Big|_{y=-\alpha} \end{cases} \tag{41}$$

From Eqs. (32) and (37), we get

$$u_o(y) = \frac{e^{-\sqrt{B}(2y+\alpha)-(1+y)\beta}}{\left(B\left(-1+e^{2\sqrt{B}(1+\alpha)}\right)(1+e^{\beta+\alpha\beta})\left(\sqrt{B}-\beta\right)\left(\sqrt{B}+\beta\right)\right)}\Big(\Big(e^{\sqrt{B}(1+y+\alpha)} - e^{\sqrt{B}(2y+\alpha)} - e^{\sqrt{B}(2+y+2\alpha)} + e^{\sqrt{B}(3y+2\alpha)} + e^{\sqrt{B}(2+2y+3\alpha)} - e^{\sqrt{B}(1+3y+3\alpha)}\Big)\big(e^{(1+y)\beta} + e^{(2+y+\alpha)\beta}\big)P\beta^2 + B\Big(e^{\sqrt{B}(2y+\alpha)+(1+y)\beta}P - e^{\sqrt{B}(2+2y+3\alpha)+(1+y)\beta}P + e^{\sqrt{B}(2y+\alpha)+(2+y+\alpha)\beta}P - e^{\sqrt{B}(2+2y+3\alpha)+(2+y+\alpha)\beta}P + e^{\sqrt{B}(2+y+2\alpha)+(1+y)\beta}(P-\delta) + e^{\sqrt{B}(1+3y+3\alpha)+(1+y)\beta}(P-\delta) + e^{\sqrt{B}(2+y+2\alpha)+(2+y+\alpha)\beta}(P-\delta) + e^{\sqrt{B}(1+3y+3\alpha)+(2+y+\alpha)\beta}(P-\delta) - e^{\sqrt{B}(2y+\alpha)+2\beta}\delta + e^{\sqrt{B}(2+2y+3\alpha)+2\beta}\delta - e^{\sqrt{B}(2y+\alpha)+(1+2y+\alpha)\beta}\delta + e^{\sqrt{B}(2+2y+3\alpha)+(1+2y+\alpha)\beta}\delta + e^{\sqrt{B}(1+y+\alpha)+(1+y)\beta}(-P+\delta) + e^{\sqrt{B}(3y+2\alpha)+(1+y)\beta}(-P+\delta) + e^{\sqrt{B}(1+y+\alpha)+(2+y+\alpha)\beta}(-P+\delta) + e^{\sqrt{B}(3y+2\alpha)+(2+y+\alpha)\beta}(-P+\delta)\Big)\Big) \tag{42}$$

It is assumed that the ε^1-functions may be expressed as follows based on Eqs. (33) and (38):

$$u_1(x,y) = f_1(y)\,\sin(x\lambda) + f_2(y)\,\cos(x\lambda) \tag{43}$$

It is assumed that the ε^1-functions may be expressed as follows based on Eqs. (34) and (39):

$$u_2(x,y) = f_3(y) + f_4(y)\,\cos(2x\lambda) + f_5(y)\,\sin(2x\lambda) \tag{44}$$

where $f_1(y), f_2(y), f_3(y), f_4(y)$, and $f_5(y)$ are defined in appendix A.

By integrating over the final two terms of the function w Taylor series expansion around the average wall locations, one may derive the formula for the volume flow rate per unit channel width. A single wavelength of corrugations is averaged to determine the final result.

$$\begin{aligned} q(x) &= \int_{y_l}^{y_u} u dy = \int_{y_l}^{-\alpha} u dy + \int_{-\alpha}^{1} u dy + \int_{1}^{y_u} u dy \\ &= \int_{-\alpha}^{1} u_0 dy + \varepsilon\left[\int_{-\alpha}^{1} u_1 dy + sin(\lambda x)(u_0(1)) - sin(\lambda x+\theta)\,u_0(-\alpha)\right] \\ &\quad + \varepsilon^2\left[\int_{-\alpha}^{1} u_2 dy + sin(\lambda x)u_1(1) - sin(\lambda x+\theta)\,u_1(-\alpha)\right. \\ &\quad \left. + \frac{sin^2(\lambda x)}{2}\left(\frac{dw_0}{dx}\Big|_{y=1}\right) - \frac{sin^2(\lambda x+\theta)}{2}\left(\frac{dw_0}{dx}\Big|_{y=-\alpha}\right)\right] + \ldots\ldots \end{aligned} \tag{45}$$

The mean velocity is given by

$$u_m = \frac{\lambda}{4\pi}\int_0^{\frac{2\pi}{\lambda}} q(x)dx = w_{0m}\left[1+\varepsilon^2\varphi^{\pm} + O(\varepsilon^4)\ldots\ldots\right], \tag{46}$$

Temperature distribution

The investigation of thermal transport characteristics related to the combined electromagnetohydrodynamic flows through a corrugated microchannel filled with a porous medium is described.

$$(\rho C_p)_{thnf}\frac{DT^*}{Dt} = k_{thnf}\nabla^2 T^* - \frac{\partial q_r}{\partial y^*} + Q_o(T^* - T_o) \tag{47}$$

The boundary conditions for the problem can be expressed as follows [1,5]:

$$T^*(x^*, y_u^*) = T^*(x^*, y_l^*) = 0$$

Assuming that the Heat writes as:

$$T^* = \Re\{\theta^*(x^*, y^*)e^{i\omega t^*}\}$$

By introducing the following dimensionless variables and substituting them into Equation (45),

$$T = \frac{\theta^* - \theta_o}{\theta_1 - \theta_o}, Rd = \frac{4\sigma^*\theta_o^3}{k^* k_f}, Nu = \frac{q_w d_1}{k_f(\theta_1 - \theta_o)}, Q = \frac{d_1^2 Q_o}{\mu_f (C_p)_f}, pr = \frac{(C_p)_f \mu_f}{k_f}$$

$$\frac{\partial^2 T}{\partial x^2} + \frac{\partial^2 T}{\partial y^2}(R) + \eta T + \Omega u = 0 \tag{48}$$

Where:

$$R = \left(1 + \frac{4}{3}\frac{Rd}{A_5}\right), \eta = \frac{prQ}{A_5} - i(Re)\frac{A_4}{A_5}pr, \Omega = \frac{A_4}{A_5}(Nu), A_4 = \frac{(\rho c_p)_{thnf}}{(\rho c_p)_f}, A_5 = \frac{k_{thnf}}{k_f}$$

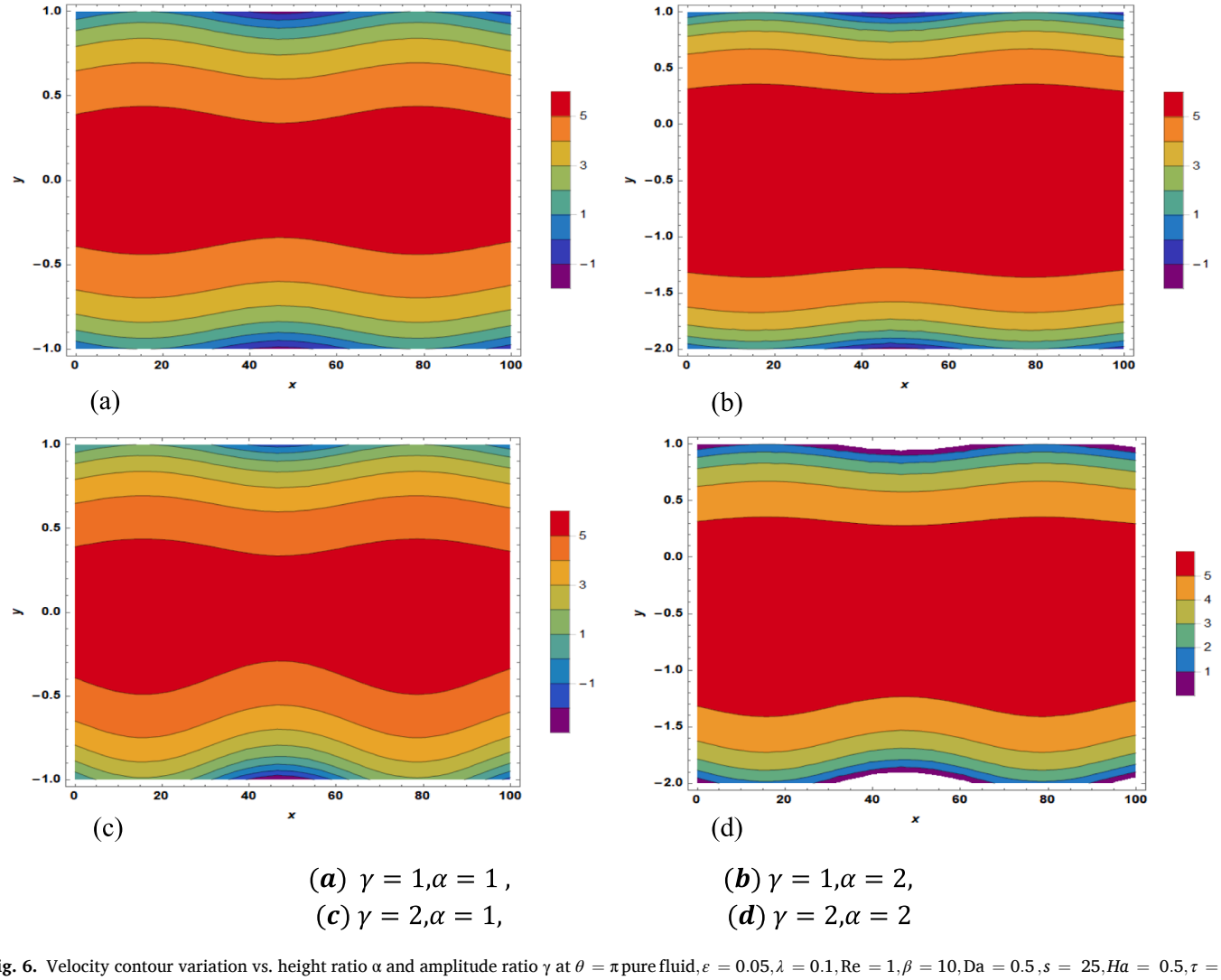

$(\boldsymbol{a})\ \gamma = 1, \alpha = 1$, $(\boldsymbol{b})\ \gamma = 1, \alpha = 2$,
$(\boldsymbol{c})\ \gamma = 2, \alpha = 1$, $(\boldsymbol{d})\ \gamma = 2, \alpha = 2$

Fig. 6. Velocity contour variation vs. height ratio α and amplitude ratio γ at $\theta = \pi$ pure fluid, $\varepsilon = 0.05, \lambda = 0.1, \mathrm{Re} = 1, \beta = 10, \mathrm{Da} = 0.5, s = 25, Ha = 0.5, \tau = 1$, $\omega\lambda_1 = 0.5\pi, \omega\lambda_2 = 0.1\pi$.

$$k_{nf} = k_f\left(\frac{k_{s_3} + 2k_f - 2\phi_3(k_f - k_{s_3})}{k_{s_3} + 2k_f + \phi_3(k_f - k_{s_3})}\right)$$

$$k_{hnf} = k_{nf}\left(\frac{k_{s_2} + 2k_{nf} - 2\phi_2(k_{nf} - k_{s_2})}{k_{s_2} + 2k_{nf} + \phi_2(k_{nf} - k_{s_2})}\right)$$

$$k_{thnf} = k_{hnf}\left(\frac{k_{s_1} + 2k_{hnf} - 2\phi_1(k_{hnf} - k_{s_1})}{k_{s_1} + 2k_{hnf} + \phi_1(k_{hnf} - k_{s_1})}\right)$$

$$(\rho c_p)_{thnf} = \Big((1 - \phi_1 - \phi_2 - \phi_3)(\rho c_p)_f\Big) + \Big(\phi_1(\rho c_p)_{s_1}\Big) + \Big(\phi_2(\rho c_p)_{s_2}\Big) + \Big(\phi_3(\rho c_p)_{s_3}\Big)$$

with the following boundary conditions:

$$T = 1 \text{ at } y_u = 1 + \varepsilon\sin(\lambda x) \tag{49}$$

$$T = 1 \text{ at } y_l = -\alpha + \gamma\,\varepsilon\,\sin(\lambda x + \theta) \tag{50}$$

The regular perturbation expansion in small values of ε can be used to describe the Heat.

$$T(x,y) = T_o(x,y) + \varepsilon T_1(x,y) + \varepsilon^2 T_2(x,y) + \ldots\ldots\ldots \tag{51}$$

By substituting Eq. (48) into Eq. (45), we get

$$\varepsilon^o : \frac{\partial^2 T_o}{\partial x^2} + \frac{\partial^2 T_o}{\partial y^2}R + \eta T_o + \Omega u_o = 0 \tag{52}$$

$$\varepsilon^1 : \frac{\partial^2 T_1}{\partial x^2} + \frac{\partial^2 T_1}{\partial y^2}R + \eta T_1 + \Omega u_1 = 0 \tag{53}$$

$$\varepsilon^2 : \frac{\partial^2 T_2}{\partial x^2} + \frac{\partial^2 T_2}{\partial y^2}R + \eta T_2 + \Omega u_2 = 0 \tag{54}$$

The boundary constraints equations (47) and (48) can be expanded in the following form using a Taylor series around the mean wall positions $y = 1$ and $y = -\alpha$.

$$1 = T(x,1) + \varepsilon\,\sin(\lambda x)\frac{\partial T}{\partial y}(x,1) + \frac{\varepsilon^2}{2}\sin^2(\lambda x)\frac{\partial^2 T}{\partial y^2}(x,1) + \ldots\ldots\ldots \tag{55}$$

$$1 = T(x,-\alpha) + \gamma\,\varepsilon\,\sin(\lambda x + \theta)\frac{\partial T}{\partial y}(x,-\alpha) + \gamma^2\frac{\varepsilon^2}{2}\sin^2(\lambda x + \theta)\frac{\partial^2 T}{\partial y^2}(x,-\alpha) + \ldots\ldots \tag{56}$$

Similarly, the associated boundary conditions given by equations (50), (51), and (52) can be further simplified by grouping terms with equal powers, as shown below.

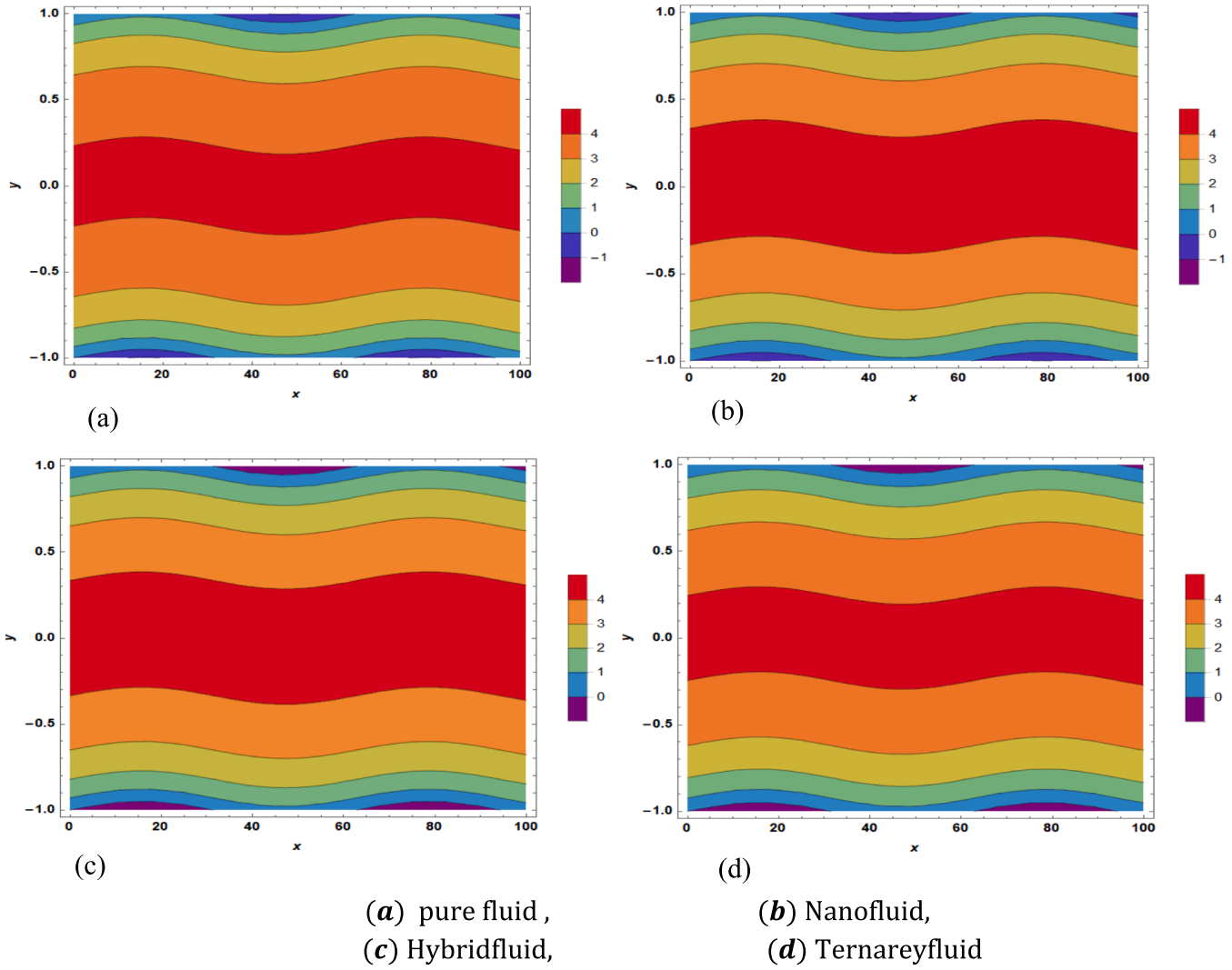

(***a***) pure fluid , (***b***) Nanofluid,
(***c***) Hybridfluid, (***d***) Ternareyfluid

Fig. 7. Velocity contour variation vs. nanoparticles concentration at $\theta = 0$ pure fluid, $\varepsilon = 0.05, \lambda = 0.1, \mathrm{Re} = 1, \alpha = 1, \beta = 10,\ \mathrm{Da} = 0.5, s = 25, Ha = 0.5, \tau = 1,$ $\omega\lambda_1 = 0.2\pi, \omega\lambda_2 = 0.1\pi$.

$$\varepsilon^o \begin{cases} T_o(x,y)\,|_{y=1} = 1 \\ T_o(x,y)\,|_{y=-\alpha} = 1 \end{cases} \tag{57}$$

$$\varepsilon^1 : \begin{cases} T_1(x,y)\,|_{y=1} = -\sin(\lambda x)\dfrac{\partial T_o(x,y)}{\partial y}\Big|_{y=1} \\ T_1(x,y)\,|_{y=-\alpha} = -\gamma\sin(\lambda x+\theta)\dfrac{\partial T_o(x,y)}{\partial y}\Big|_{y=-\alpha} \end{cases} \tag{58}$$

From Eqs. (50) and (57), we get

$$T_o(y) = \frac{(e^{-\sqrt{B}(2y+7\alpha)-(y+3\alpha)\beta}\,\mathrm{Csc}[\frac{(1+\alpha)\sqrt{\eta}}{\sqrt{R}}]}{(B(-1+e^{2\sqrt{B}(1+\alpha)})(1+e^{\beta+\alpha\beta})(B-\beta^2)(\sqrt{B}\sqrt{R}-i\sqrt{\eta})} B_1 \times(\sqrt{R}\beta-i\sqrt{\eta})(\sqrt{B}\sqrt{R}+i\sqrt{\eta})(\sqrt{R}\beta+i\sqrt{\eta})\eta) \tag{60}$$

From Eqs. (51) and (58) we assume that the ε^1-functions can be written as:

$$T_1(x,y) = \vartheta_1(y)\,\mathrm{Sin}(x\lambda) + \vartheta_2(y)\,\mathrm{Cos}(x\lambda) \tag{61}$$

From Eqs. (52) and (59) we assume that the ε^1-functions can be

$$\varepsilon^2 : \begin{cases} T_2(x,y)\,|_{y=1} = -sin(\lambda x)\dfrac{\partial T_1(x,y)}{\partial y}\Big|_{y=1} - \dfrac{sin^2(\lambda x)}{2}\dfrac{\partial^2 T_o(x,y)}{\partial y^2}\Big|_{y=1} \\ T_2(x,y)\,|_{y=-\alpha} = -\gamma sin(\lambda x+\theta)\dfrac{\partial T_1(x,y)}{\partial y}\Big|_{y=-\alpha} - \gamma^2\dfrac{sin^2(\lambda x+\theta)}{2}\dfrac{\partial^2 T_o(x,y)}{\partial y^2}\Big|_{y=-\alpha} \end{cases} \tag{59}$$

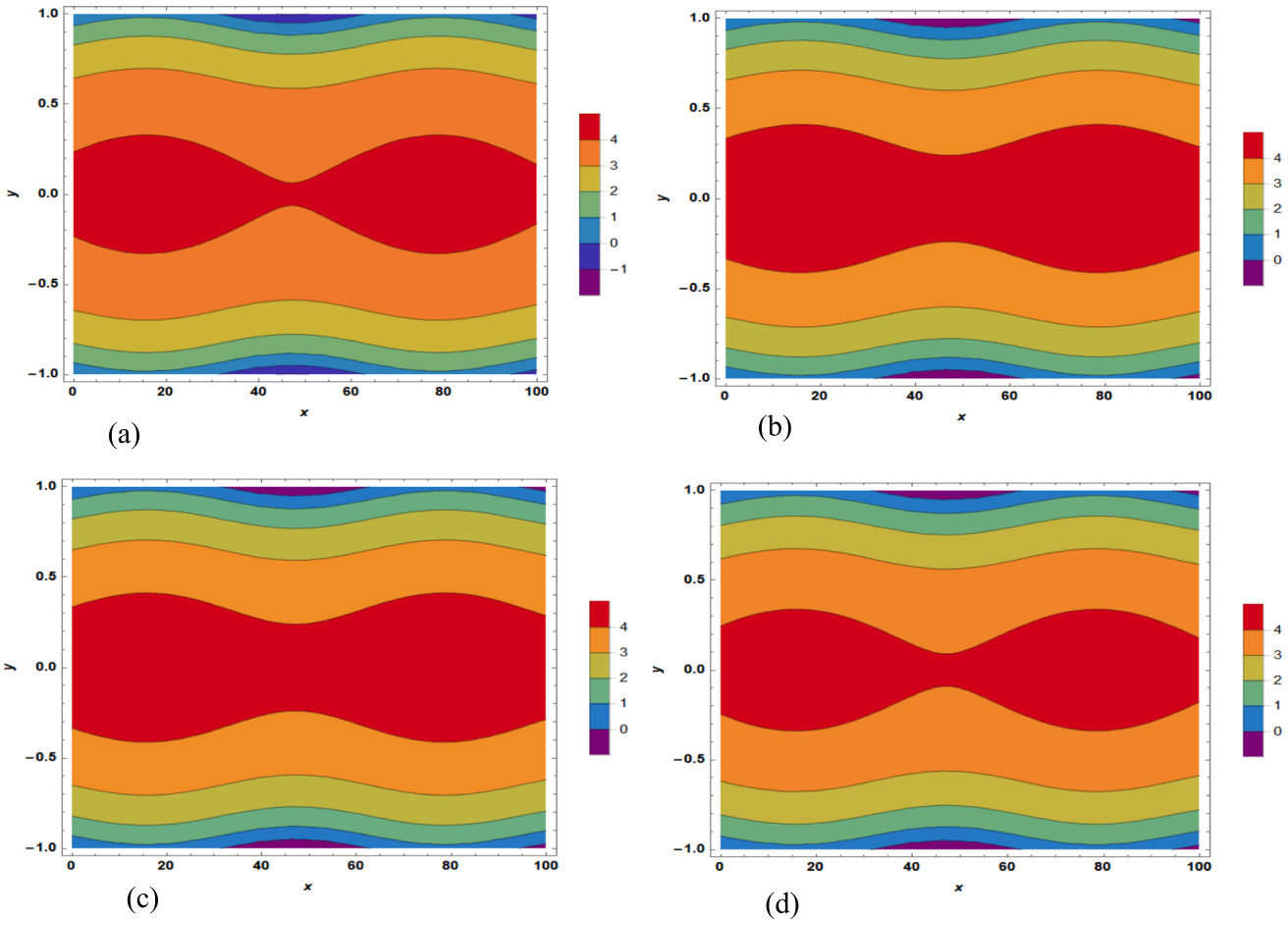

Fig. 8. Velocity contour variation vs. nanoparticles concentration at..$\theta = \pi$ pure fluid, $\varepsilon = 0.05, \lambda = 0.1, \mathrm{Re} = 1, \alpha = 1, \beta = 10, \mathrm{Da} = 0.5, s = 25, Ha = 0.5, \tau = 1$, $\omega\lambda_1 = 0.2\pi, \omega\lambda_2 = 0.1\pi$.

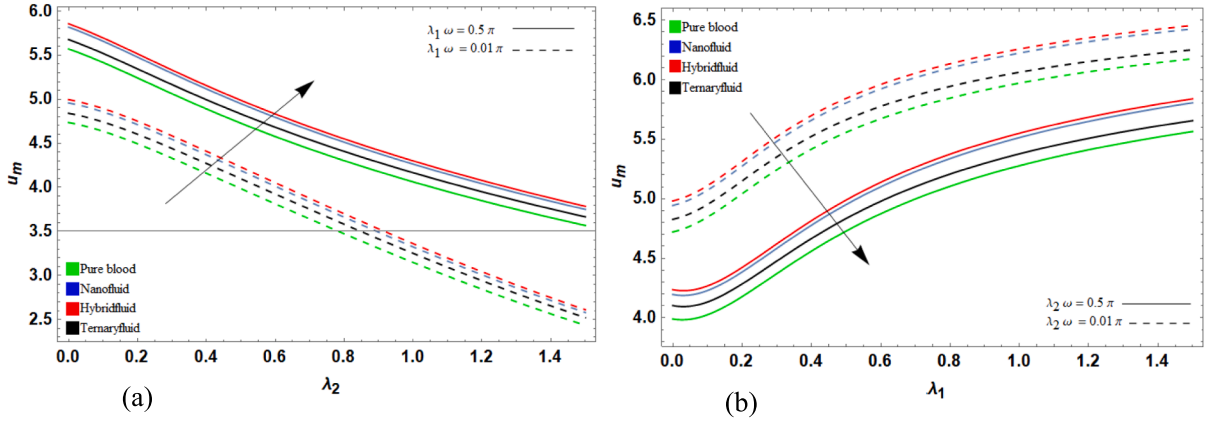

Fig. 9. Mean velocity for..$\theta = 0, \pi, \varepsilon = 0.05, \lambda = 0.1, \mathrm{Re} = 2, \alpha = 1, \beta = 10, \mathrm{Da} = 0.1, s = 50, Ha = 1.5, \tau = 2$$(a)$variation of relaxation time λ_1 (b)variation of retardation time λ_2.

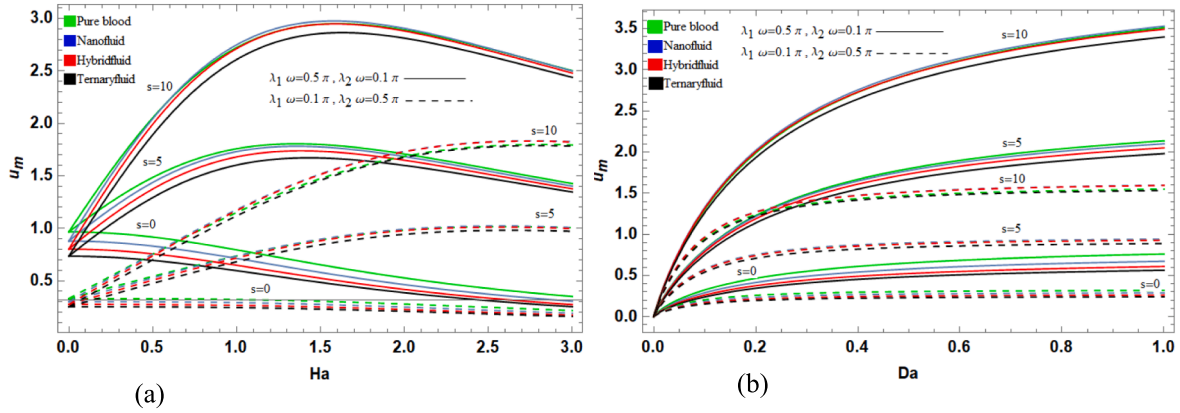

Fig. 10. Mean velocity for $\theta = 0, \pi, \varepsilon = 0.05, \lambda = 0.1, \mathrm{Re} = 2, \alpha = 1, \beta = 10, \tau = 2$ (a)variation of Hartmann number Ha, Da $= 0.5$ (b)variation of porous medium Da, Ha $= 1.5$

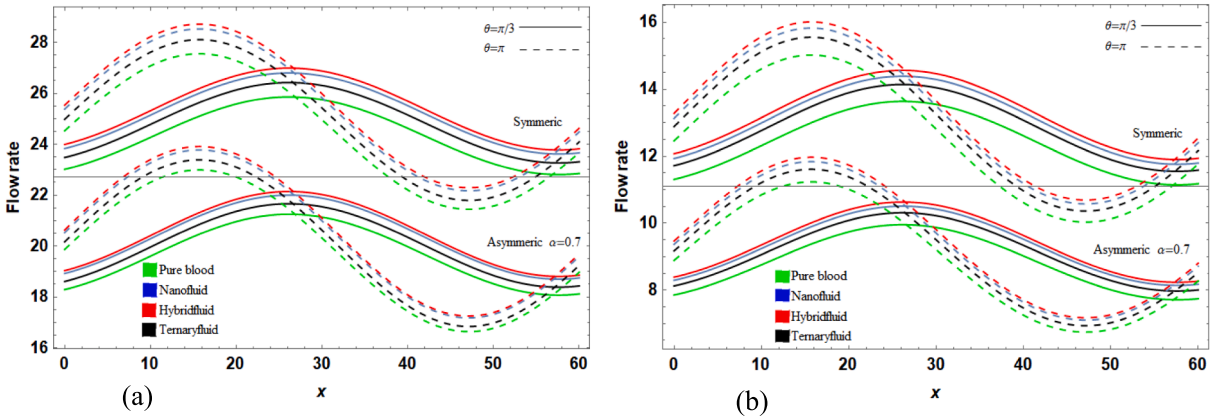

Fig. 11. Flow rate variation vs. nanoparticles concentration at $\theta = 0, \pi$ pure fluid, $\varepsilon = 0.05, \lambda = 0.1, \alpha = 1, \beta = 10, \tau = 2$.

written as:

$$T_2(x,y) = \vartheta_3(y) + \vartheta_4(y)\,\mathrm{Cos}(2x\lambda) + \vartheta_5(y)\,\mathrm{Sin}(2x\lambda) \tag{62}$$

where $B_1, \vartheta_1(y), \vartheta_2(y), \vartheta_3(y), \vartheta_4(y)$, and $\vartheta_5(y)$ are defined in appendix A.

Discussion of the Outcome

In this section, we visually examine the behavior of blood fluid supported by nanoparticles *Au*, Fe_3o_4 and *SWCNTs* as it flows through corrugated walls. The problem was simulated using a series of partial differential equations and analytically solved using the perturbation method. Approximate analytical solutions were obtained using Mathematica software. We investigated the flow rate and heat transfer rate at various locations in the microchannel.

Additionally, the values of non-dimensional parametric variables were calculated based on the information provided in Table 2.

It is important to note that the height of the channel, *H*, is approximately $40\mu m$ for microfluidic investigations. The impact of wavy roughness and porosity on electromagnetically driven flow and temperature in the microchannel was examined using the following key parameter values, as referenced in [8,12,15].

$O(\rho) \sim 1 \times 10^3 - 5.91 \times 10^3 kgm^{-3}$,

$O(\mu) \sim 0.001 kgms^{-1}$,

$O(By) \sim 1 - 50T$,

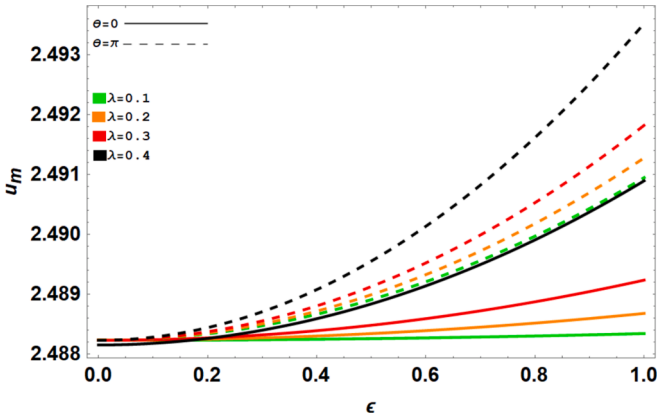

Fig. 12. Mean velocity and $\varepsilon\ \theta = 0, \pi, \lambda = 0.1, \mathrm{Re} = 2, \alpha = 1, \beta = 10, \tau = 1, s = 50, Ha = 0.5, \tau = 1, \omega\lambda_1 = \pi, \omega\lambda_2 = 0.1\pi$.

$O(Ex) 0 - 10^4 Vm^{-1}$,

$O(Ez) \sim 0 - 10^4 Vm^{-1}$,

$O(P1) \sim 10\dfrac{Pa}{m}$,

$O(Sj) \sim (-1) - (-15)$.

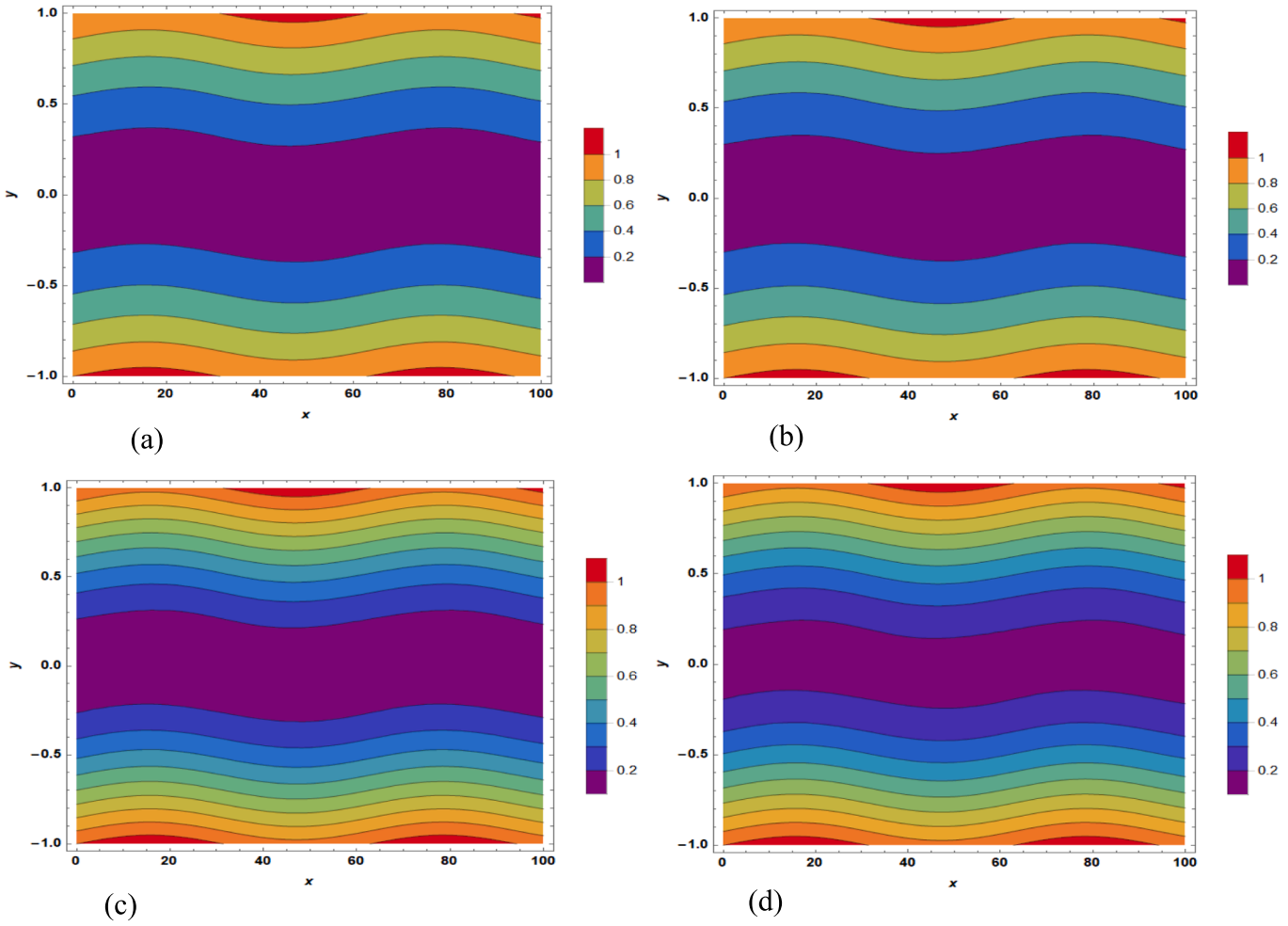

Fig. 13. Contour plot for Heat distribution for θ=0, ε=0.05, λ=0.1, Re=1.5, α=1, γ=1, β=10, Ha=1.5, Da=0.1, s=50, τ = 2, ωλ_1 = π, ωλ_2 = 0.1π, Rd=5,pr=21, Q=0.1,Nu=0.5(a) pure fluid, (b)Nanofluid, (c)Hybridfluid,(d)Ternareyfluid

In order to verify the accuracy of the obtained results, a comparison is made with the previously published data using the same conditions. The comparison can be found in Table 3, with the following parameter settings: $s = 5, \beta = 0, \lambda = 0.1, \phi_1 = \phi_2 = \phi_3 = 0, \alpha = 1, \gamma = 1, \omega\lambda_1 = 1.5\pi, \omega\lambda_2 = 0.1\pi$ and $\epsilon = 0.1, Da = \infty$.

Behavior of flow velocity

This section gives a thorough description of how the channel's speed changes in relation to some of the crucial research parameters. At different concentrations of nanoparticles, velocity behavior changes, When the electric field $s = 0$, there is no Lorentz force acting on the fluid, as shown in Fig. 2-a. Instead, the pulse pressure force and magnetic field will primarily affect blood flow. The velocity of pure fluid without any particles will be greater than the velocity of blood containing Fe_3O_4 particles (Nanofluid) $\phi_2 = 5\%$. this is due to the collisions between the Fe_3O_4 particles and each other, which create resistance to flow within the channel, resulting in a decrease in velocity. When gold $\phi_3 = 5\%$ and Fe_3O_4 particles $\phi_2 = 5\%$. (hybrid fluid) are added, the collisions between the particles and each other increase, further reducing the velocity. Adding single-walled carbon particles $\phi_1 = 5\%$ (ternary fluid) also reduces the velocity for the same reason.

When there is a strong electric field, the velocity of pure fluid decreases (Fig. 2-b). This is because the Lorentz force will act to attract the gold and Fe_3O_4 particles, which acquire electric charges, thus giving greater blood flow. These particles aid in propelling the blood fluid and surmounting their resistance. The velocity will be higher when the relaxation time is greater than the retardation time.

In Fig. 3-a, when the relaxation time was less than the retardation time, the velocity distribution within the channel was consistent. However, in Fig. 3-b, when the relaxation time was greater than the retardation time, the flow became more turbulent, which affected the velocity distribution within the channel. The Reynolds number is critical in determining the type of flow within the channel. At a lower Reynolds number, the flow is more streamlined, leading to a noticeable increase in velocity. As the Reynolds number increases, the velocity decreases. The highest blood flow velocity occurs when both Fe_3O_4 nanoparticles and gold particles (hybrid fluid) are present in the presence of an electric field, as shown in the figure. This suggests that the combination has a positive effect on increasing velocity.

Fig. 4 illustrates the difference between the symmetric channel and the asymmetric channel as the values of relaxation time and retardation time change. Changes in the values of relaxation time and retardation time result in differences in the velocity between the symmetric channel and the asymmetric channel. Figs. 5 and 6 show the velocity contours for conduit walls with the same or different phase angle after changing both the height ratio (α) and amplitude ratio (γ). As the height ratio increases, the undulating motion becomes more fluid and decays at a faster speed. Furthermore, a significant disruption in velocity is followed by a more pronounced undulation, particularly in the bottom section of the conduit, with an increase in the amplitude ratio. By comparing Figs. 3 and 4, one can see that the existence of a phase angle between the walls results in symmetry and intensity in the velocity movement with improved flow.

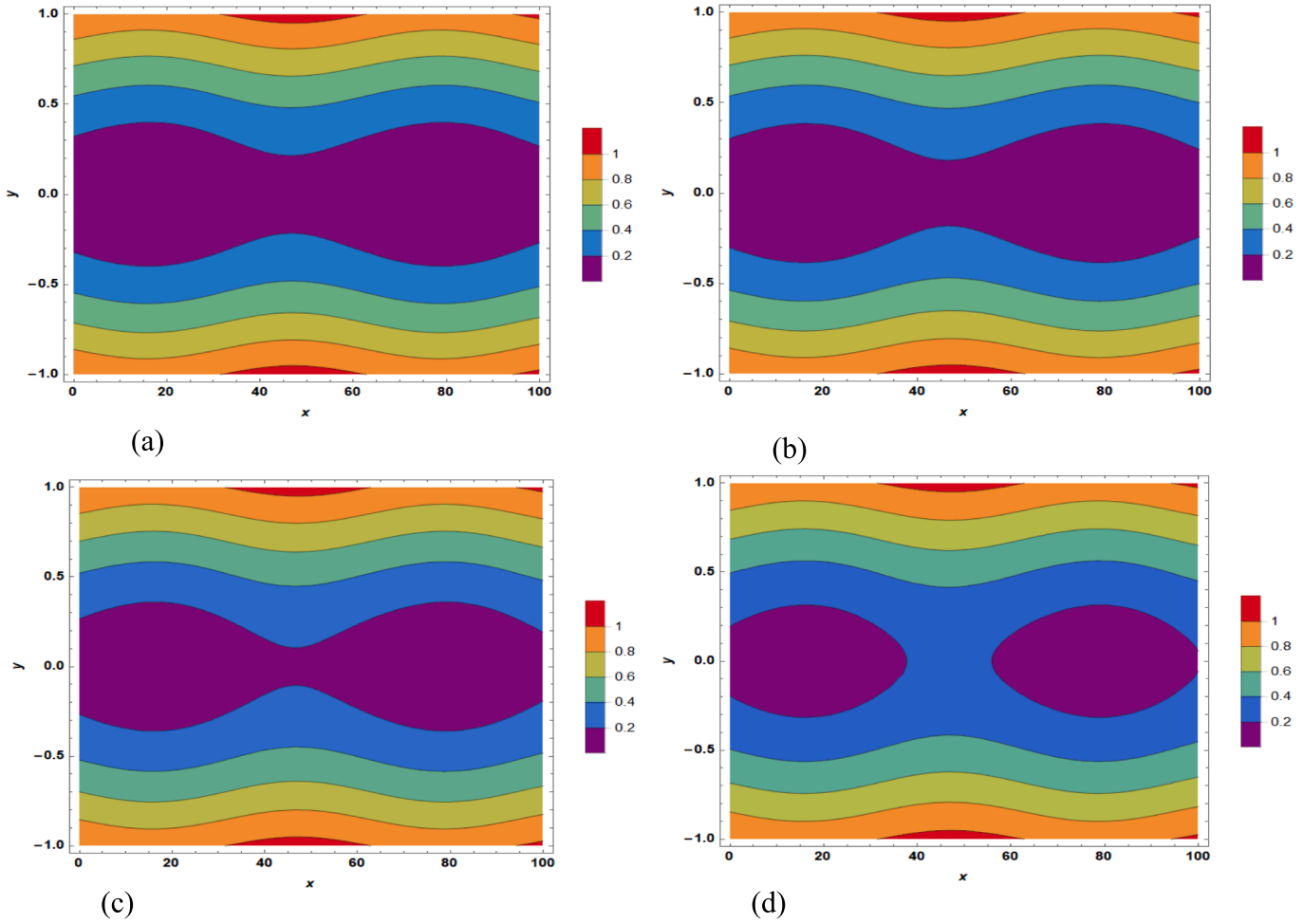

Fig. 14. Contour plot for Heat distribution for θ=π,ε=0.05,λ=0.1,Re=1.5,α=1,γ=1,β=10,Ha=1.5,Da=0.1, s=50, τ=2, ωλ_1=π,ωλ_2=0.1π, Rd=5,pr=21,Q=0.1, Nu=0.5(a) pure fluid, (b) Nanofluid, (c) Hybridfluid, (d) Ternareyfluid.

Figs. 7 and 8 depict the velocity contour distribution inside the conduit with varying nanoparticle concentration at two distinct phase angles ($\theta = 0 and \theta = \pi$). When one or two types of nanoparticles support pure fluid at the same phase and different phase angles, the contour velocity clearly increases; however, the addition of three nanoparticles appears to cause an odd phenomenon, as the contour area begins to decrease again. With a phase angle ($\theta = \pi$), the boluses are formed in the middle of the conduit, forming high flow rings. We limit these boluses by using one or two nanoparticles, but we notice their re-formation when we support the blood with three types of nanoparticles.

See Fig. 9-a illustrates the relationship between the mean velocity and the relaxation time. As observed, the mean velocity increases with relaxation time. Fig. 9-b shows the relationship between the mean velocity and the relaxation time, showing that the average velocity decreases as the relaxation time increases. In both cases, the electric field was $s = 50$, which provides a large Lorentz force. The result was that the fluid's mean velocity was the highest when mixed with 0.05% each of Fe_3O_4 and gold nanoparticles. To see the effect of the electric field and its impact on the hybrid fluid, we used some small electric fields, as shown in Fig. 10-a. It shows the relationship between the mean velocity and the Hartmann number. As the electric field increases, the velocity increases, demonstrating a clear effect on the nanofluids. It is also evident that the relaxation time and the relaxation time have an effect on the mean velocity of the fluid, whether the channel walls are in the same phase or a different phase. Fig. 10-b illustrates the relationship between the mean velocity and the porous medium, the change in electric fields, and their clear influence on nanofluid motion. Looking at the flow rate in Fig. 11-a, we can confirm that the symmetric channel provides a higher flow rate compared to the asymmetric channel. Changing the angle θ illustrates the fluid flow's wave motion. If we look at Fig. 11-b, we notice that the flow rate decreases for the same parameters, except for the relaxation time and the retardation time. If the relaxation time decreases while the retardation time increases, the velocity decreases, and consequently, the flow rate decreases. In Fig. 12, the mean velocity increases with the increase in wavelength. We also observe that the wall wave, when different of phase, increases compared to its counterpart when in phase.

Fluid temperature behavior

When studying the effects of the parameters on the temperature gradients in the channel for both symmetric and asymmetric cases of blood fluid, we refer to Figs. 13 and 14. These figures illustrate the contour in the case of a symmetric channel with walls in the same phase, as well as in different phases, respectively. In Figs. 13-a, we see the contour for blood without nanoparticles, showing a temperature gradient where the temperature decreases in the middle of the channel. Meanwhile, Figs. 13-b represents the temperature distribution of blood with Fe_3O_4 nanoparticles at a concentration of 0.05, where the addition of nanoparticles leads to a reduction in temperature. Looking at Figs. 13-c, we notice that the contour lines have become closer together due to the addition of gold nanoparticles at a concentration of 0.05 to the Fe_3O_4 particles. In Figs. 13-d, the blood contains three types of nanoparticles gold, SWCNTs, and Fe_3O_4 at equal concentrations of 0.05. The impact is

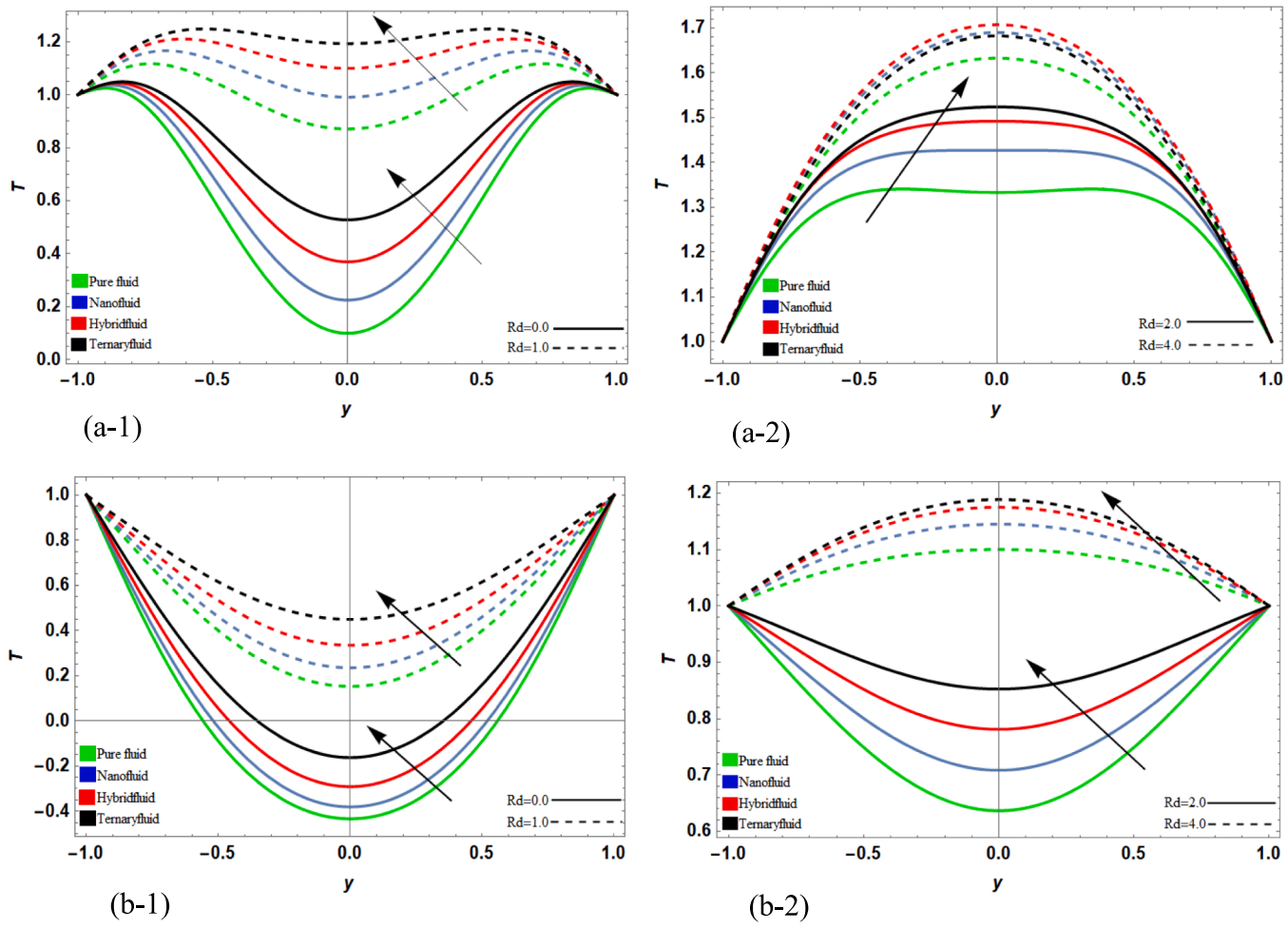

Fig. 15. The Heat distribution vs. the nanoparticles concentration for θ=0,π,ε=0.01,λ=0.1,Re=2,α=1,γ=1,β=10,Ha=1.5,Da=0.1, s=50, τ=2, pr=21, Q=0.1, Nu=3, (a)ωλ_1=π, ωλ_2=0.1π, (b)ωλ_1=0.1π,ωλ_2=π.

evident, as this combination causes the contour lines to converge, resulting in a decreased temperature of the fluid in the middle of the channel.

When there is a phase difference between the walls of the channel, we observe in Figs. 14-a that the temperature of the blood without nanoparticles decreases in the middle of the channel. However, along the length of the channel, there is a fluctuation in temperature, with increases in some areas and decreases in others. In Figs. 14-b, the temperature decreases after adding a concentration of 0.05 of Fe_3O_4 nanoparticles, with a noticeable fluctuation in the middle. Additionally, in Figs. 14-c, nanoparticles of both gold and Fe_3O_4 were added at a concentration of 0.05 each. When SWCNTs nanoparticles were added at a concentration of 0.05, along with gold and Fe_3O_4 nanoparticles to the fluid, the temperature decreased in some areas while increasing in others along the length of the channel, as also seen in Figs. 14-d.

In Figs. 15-a, the relaxation time was greater than the retardation time. We observe that the non-effect of the radiation coefficient on the channel may affect the blood temperature and cause a thermal response in the middle of the channel. As the radiation increases, the blood temperature in the middle of the channel also increases.

As seen in Figs. 15-b, the retardation time was greater than the relaxation time, which resulted in lower temperatures as the radiation decreased, and higher temperatures as the radiation increased.

The Hartmann number enhances the effect of temperature, and it increases as the Hartmann number increases. We observe this change with the intensity of the electric field, as seen in the difference between Fig. 16-a and (16-b). The results shown in Fig. 16-c and (16-d) also demonstrate an increase in temperature as the channel width decreases. Additionally, there appears to be a difference in the impact on nanoparticles, as the blood containing nanoparticles exhibits lower temperatures compared to the blood without nanoparticles.

Conclusion

By carefully tuning the nanoparticle properties and conduit geometry, it is possible to optimize the flow characteristics for various biomedical applications, such as targeted drug delivery, disease diagnostics, and tissue engineering. The findings from this study provide valuable insights into the design and control of nanoparticle-based microfluidic systems for enhanced performance and functionality. These finding summered in the following points:

- The EMHD velocity in phase experiences an increase as $\lambda_1\omega$ rises, largely attributed to the pronounced elastic effects. Conversely, it diminishes when $\lambda_2\omega$ increases, primarily due to the significant retardation effects characteristic of Jeffrey fluids.
- The presence of the magnetic field leads to a significant alteration in the velocity behavior within the conduit. This effect is particularly pronounced as the Hartmann number increases, influencing the flow dynamics and the relationship between the parameters of the Jeffrey fluid. The interactions between the magnetic field and the fluid properties result in notable changes in both in-phase and out-of-phase velocity profiles.

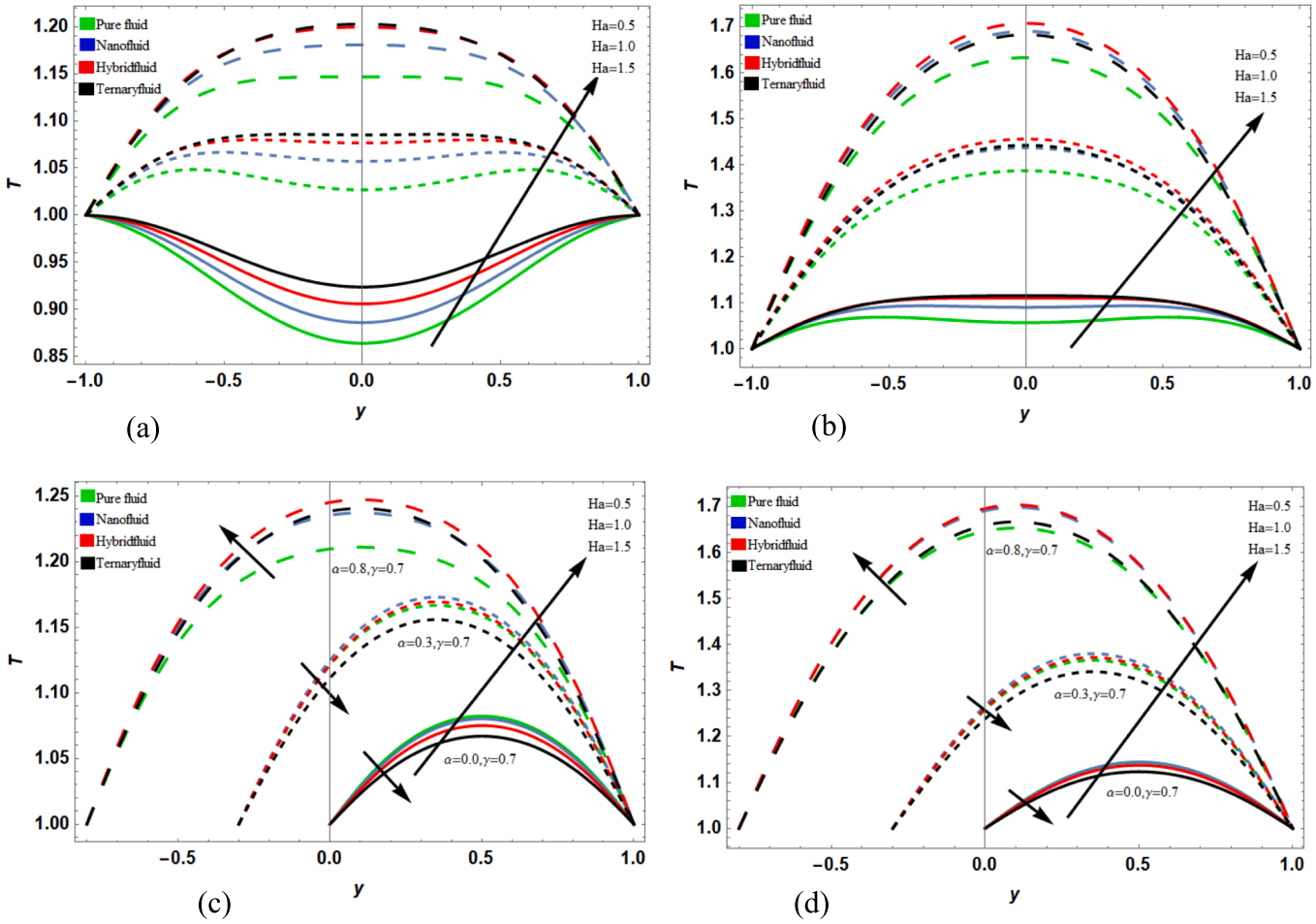

Fig. 16. The Heat distribution vs. the nanoparticles concentration for θ=0,π,ε=0.01,λ=0.1,Re=2,α=1,γ=1,β=10,Da=0.1, s=50, τ=2, pr=21, Q=0.1, Nu=3,(a)s=25, (b)s=50.

- Introducing an electric field can either decrease or increase the fluid velocity, depending on the relaxation and retardation times of the charged nanoparticles.
- The study of the effects of parameters on temperature gradients in blood flow channels, both symmetric and asymmetric, reveals that the presence of nanoparticles significantly contributes to reducing temperature.
- When there is a phase difference between the channel walls, noticeable fluctuations in temperature occur, with a significant reduction observed after adding Fe3O4 nanoparticles.
- Furthermore, an increase in the Hartmann number enhances thermal effects, with temperature rising alongside the intensity of the electric field.
- Lastly, the presence of nanoparticles in blood consistently results in lower temperatures compared to blood without them. This effect is further influenced by the asymmetry of the channel, which plays a crucial role in the overall thermal dynamics, demonstrating how channel geometry interacts with nanoparticle behavior to enhance thermal properties.

CRediT authorship contribution statement

Mohamed S. Abdel-wahed: Writing – review & editing, Software, Methodology, Formal analysis. **Khaled S. Mekheimer:** Writing – review & editing, Investigation, Conceptualization. **Ahmed Y. Sayed:** Writing – original draft, Validation, Investigation, Formal analysis. **Shaaban I. Ahmed:** Writing – original draft, Software, Formal analysis, Data curation, Conceptualization.

Declaration of competing interest

The authors declare that they have no known competing financial interests or personal relationships that could have appeared to influence the work reported in this paper.

Acknowledgements

The authors extend their appreciation to the Kingdom University, Kingdom of Bahrain, for funding this research work under Grant Number (KU-SRU- 2024-04).

Data availability

Data will be made available on request.

References

[1] Hussain Z, et al. A mathematical model for radiative peristaltic flow of Jeffrey fluid in curved channel with Joule heating and different walls: Shooting technique analysis. Ain Shams Eng J 2022;13(5):101685.
[2] Kumar SR, Ahamad NA. Peristaltic hemodynamic Jeffery fluid through a tapered channel with heat and mass transfer under the influence of radiation–blood flow model. International Journal of Hybrid Information Technology 2016;9(11): 353–68.

[3] R. Latha, B. R. Kumar, and O. D. Makinde, "Effects of heat dissipation on the peristaltic flow of Jeffery and Newtonian fluid through an asymmetric channel with porous medium," in *Defect and Diffusion Forum*, 2018, vol. 387, pp. 218-243: Trans Tech Publ.

[4] Manjunatha G, Rajashekhar C, Prasad K, Vaidya H. Peristaltic flow of a Jeffery fluid over a porous conduit in the presence of variable liquid properties and convective boundary. International Journal of Thermofluid Science and Technology 2019;6:19060201.

[5] Manjunatha G, Rajashekhar C, Vaidya H, Prasad K, Vajravelu K. Impact of heat and mass transfer on the peristaltic mechanism of Jeffery fluid in a non-uniform porous channel with variable viscosity and thermal conductivity. J Therm Anal Calorim 2020;139(2):1213–28.

[6] Rajashekhar C, et al. Impact of electroosmosis and wall properties in modelling peristaltic mechanism of a Jeffrey liquid through a microchannel with variable fluid properties. Inventions 2021;6(4):73.

[7] Tanveer A, Hayat T, Alsaedi A. Peristaltic flow of MHD Jeffery nanofluid in curved channel with convective boundary conditions: a numerical study. Neural Comput & Applic 2018;30:437–46.

[8] Q. Liu, Y. Jian, and L. Yang, "Alternating current electroosmotic flow of the Jeffreys fluids through a slit microchannel," *Physics of fluids,* vol. 23, no. 10, 2011.

[9] Rashid M, Nadeem S. EMHD flow through microchannels with corrugated walls in the presence of nanofluid. Can J Phys 2019;97(7):701–20.

[10] Reza M, Rana A, Shit G. Thermo-fluidic transport of electromagnetohydrodynamic flow in a corrugated porous medium microchannel. The European Physical Journal plus 2021;136(5):496.

[11] Sayed AY, Ahmed SI, Mekheimer KS, Abdel-wahed MS. Electromagnetohydrodynamic effects with single-walled carbon nanotubes particles in a corrugated microchannel. Chaos Solitons Fractals 2023;168:113126.

[12] Si D, Jian Y. Electromagnetohydrodynamic (EMHD) micropump of Jeffrey fluids through two parallel microchannels with corrugated walls. J Phys D Appl Phys 2015;48(8):085501.

[13] Xuan X, Li D. Electroosmotic flow in microchannels with arbitrary geometry and arbitrary distribution of wall charge. J Colloid Interface Sci 2005;289(1):291–303.

[14] M. Abdel-Wahed and M. Akl, "Effect of hall current on MHD flow of a nanofluid with variable properties due to a rotating disk with viscous dissipation and nonlinear thermal radiation," *AIP Advances,* vol. 6, no. 9, 2016.

[15] Abdel-Wahed M, Elbashbeshy E, Emam T. Flow and heat transfer over a moving surface with non-linear velocity and variable thickness in a nanofluids in the presence of Brownian motion. Appl Math Comput 2015;254:49–62.

[16] Abdel-Wahed M, Emam T. MHD boundary layer behaviour over a moving surface in a nanofluid under the influence of convective boundary conditions. Journal of Mechanical Engineering 2017;63(2):119–28.

[17] Abdel-Wahed MS. Lorentz force effect on mixed convection micropolar flow in a vertical conduit. The European Physical Journal plus 2017;132:1–11.

[18] Abdel-Wahed MS. Rotating ferro-nanofluid over stretching plate under the effect of hall current and joule heating. J Magn Magn Mater 2017;429:287–93.

[19] Abdel-wahed MS. Flow and heat transfer of a weak concentration micropolar-nanofluid over steady/unsteady-moving surface. Appl Phys A 2017;123:1–10.

[20] Abdel-Wahed MS. Nonlinear Rosseland thermal radiation and magnetic field effects on flow and heat transfer over a moving surface with variable thickness in a nanofluid. Can J Phys 2017;95(3):267–73.

[21] Abdel-wahed MS. Magnetohydrodynamic Ferro-Nano fluid flow in a semi-porous curved tube under the effect of hall current and nonlinear thermal radiative. J Magn Magn Mater 2019;474:347–54.

[22] El-Bashbeshy E-S, Emam TG, Abdel-Wahed MS. The effect of thermal radiation, heat generation and suction/injection on the mechanical properties of unsteady continuous moving cylinder in a nanofluid. Therm Sci 2015;19(5):1591–601.

[23] Mohammadein S, Raslan K, Abdel-Wahed M, Abedel-Aal EM. KKL-model of MHD CuO-nanofluid flow over a stagnation point stretching sheet with nonlinear thermal radiation and suction/injection. Results Phys 2018;10:194–9.

[24] Raslan K, Mohamadain S, Abdel-wahed M, Abedel-aal EM. MHD steady/unsteady porous boundary layer of Cu–water nanofluid with micropolar effect over a permeable surface. Appl Sci 2018;8(5):736.

[25] Sayed AY, Abdel-wahed MS. Entropy analysis for an MHD nanofluid with a microrotation boundary layer over a moving permeable plate. The European Physical Journal plus 2020;135(1):106.

[26] Abdel-Wahed M, Sayed A. Hybrid/mono-carbon nanotubes–water flow in a peristaltic curved channel with viscous dissipation. The European Physical Journal plus 2021;136(9):979.

[27] Alqarni AJ, Abo-Elkhair R, Elsaid EM, Abdel-Aty A-H, Abdel-wahed MS. Effect of magnetic force and moderate Reynolds number on MHD Jeffrey hybrid nanofluid through peristaltic channel: application of cancer treatment. The European Physical Journal plus 2023;138(2):1–30.

[28] Elsaid EM, Abdel-Wahed MS. Impact of hybrid nanofluid coolant on the boundary layer behavior over a moving cylinder: numerical case study. Case Stud Therm Eng 2021;25:100951.

[29] Elsaid EM, Abdel-Wahed MS. Thermal evaluation of MHD boundary-layer flow of hybridity nanofluid via a 3D sinusoidal cylinder. ZAMM-Journal of Applied Mathematics and Mechanics/zeitschrift Für Angewandte Mathematik Und Mechanik 2024;104(1):e202300186.

[30] Elsaid EM, Sayed A, Abdel-wahed MS. Electromagnetohydrodynamic unsteady blood flow with ternary nanoparticles in a vertical irregular peristaltic flow: an exact treatment. J Therm Anal Calorim 2023;148(24):14163–81.

[31] Elsaid EM, Sayed AA, Abdel-wahed MS. Entropy study of electromagnetohydrodynamic trihybrid nanofluid flow within non-uniform peristaltic across microchannel. ZAMM-Journal of Applied Mathematics and Mechanics/zeitschrift Für Angewandte Mathematik Und Mechanik 2024;104(3):e202300269.

[32] Ali A, Umar M, Bukhari Z, Abbas Z. Pulsating flow of a micropolar-Casson fluid through a constricted channel influenced by a magnetic field and Darcian porous medium: A numerical study. Results Phys 2020;19:103544.

[33] Govindarajulu K, Subramanyam Reddy A, Rajkumar D, Thamizharasan T, Dinesh Kumar M, Sekhar KR. Numerical investigation on MHD non-Newtonian pulsating Fe 3 O 4-blood nanofluid flow through vertical channel with nonlinear thermal radiation, entropy generation, and Joule heating. Numer Heat Transf A Appl 2024:1–20.

[34] Somasundaram R, Subramanyam Reddy A. Pulsating flow of electrically conducting couple stress nanofluid in a channel with ohmic dissipation and thermal radiation–Dynamics of blood. Proceedings of the Institution of Mechanical Engineers, Part e: Journal of Process Mechanical Engineering 2021;235(6):1895–909.

[35] Subramanyam Reddy A, Thamizharasan T, Rushi Kumar B, Ramachandra Prasad V, Jagadeshkumar K. A comparative study on pulsating flow of Au+ SWCNT/blood and Au+ MWCNT/blood based Jeffrey hybrid nanofluid in a vertical porous channel with entropy generation. Numer Heat Transf A Appl 2023:1–17.

[36] Sayed AY, Ahmed SI, Mekheimer S, Abdel-wahed MS. Investigating the Impact of Magnetic Fields and Pulsating Pressure on Non-Newtonian Fluid Flow in Symmetric/Asymmetric Corrugated Microchannels. Engineering Research Journal 2023;179:43–67.

[37] Nazir MW, Javed T, Ali N, Nazeer M, Khan MI. Theoretical investigation of thermal analysis in aluminum and titanium alloys filled in nanofluid through a square cavity having the uniform thermal condition. Int J Mod Phys B 2022;36(22):2250140.

[38] Chu YM, Hashmi MS, Khan N, Khan SU, Khan MI, Kadry S, et al. Thermophoretic particles deposition features in thermally developed flow of Maxwell fluid between two infinite stretched disks. J Mater Res Technol 2020;9(6):12889–98.

[39] Numerical and scale analysis of non-Newtonian fluid (Eyring-Powell) through pseudo-spectral collocation method (PSCM) towards a magnetized stretchable Riga surface.

[40] Zhao TH, Khan MI, Qayyum S, Kumar RN, Chu YM, Prasannakumara BC. Comparative study of ferromagnetic hybrid (manganese zinc ferrite, nickle zinc ferrite) nanofluids with velocity slip and convective conditions. Phys Scr 2021;96(7):075203.

[41] Abdel-wahed MS, Ahmed SI, Mekheimer KS, Sayed AY. "Entropy generation analysis of a micropolar fluid in a corrugated channel with convective and slip conditions" *Case Studies*. Therm Eng 2024;57:104283.

[42] Yu-Fei We, Hai-Jun Wang, Yong-Jun Jian, "Pressure Oscillating Flow in Corrugated Parallel Channel" *Journal of Physics* 66(2016) 104283.

[43] D. Rajkumar and A. Subramanyam Reddy, "Pulsating electrically conducting flow of Au/SWCNTs-blood micropolar nanofluid in a porous channel with Ohmic heating, thermal radiation," Phys. Scr., vol. 96, no. 12, 2021.